Title

Metabolic and Organelle Morphology Defects in Mice and Human Patients Define Spinocerebellar Ataxia Type 7 as a Mitochondrial Disease.

Journal

Cell reports, 26(5)

ISSN

2211-1247

Authors

Ward, Jacqueline M
Stoyas, Colleen A
Switonski, Pawel M
et al.

Publication Date

2019

DOI

10.1016/j.celrep.2019.01.028

Peer reviewed

HHS Public Access

Author manuscript

Cell Rep. Author manuscript; available in PMC 2019 March 15.

Published in final edited form as:

Cell Rep. 2019 January 29; 26(5): 1189–1202.e6. doi:10.1016/j.celrep.2019.01.028.

Metabolic and Organelle Morphology Defects in Mice and Human Patients Define Spinocerebellar Ataxia Type 7 as a Mitochondrial Disease

Jacqueline M. Ward[1], **Colleen A. Stoyas**[2], **Pawel M. Switonski**[2,3], **Farid Ichou**[4], **Weiwei Fan**[5], **Brett Collins**[5], **Christopher E. Wall**[5], **Isaac Adanyeguh**[6], **Chenchen Niu**[2], **Bryce L. Sopher**[7], **Chizuru Kinoshita**[8], **Richard S. Morrison**[8], **Alexandra Durr**[6,9], **Alysson R. Muotri**[1,10,11], **Ronald M. Evans**[4,12], **Fanny Mochel**[6,9], and **Albert R. La Spada**[1,10,11,13,14,15,16,17,*]

[1]Department of Pediatrics, University of California, San Diego, La Jolla, CA 92093, USA [2]Department of Neurology, Duke University School of Medicine, Durham, NC 27710, USA [3]Department of Molecular Biomedicine, Institute of Bioorganic Chemistry, Polish Academy of Sciences, Noskowskiego 12/14 Str., 61-704 Poznan, Poland [4]Metabolomics Core Facility, Institute of Cardiometabolism and Nutrition, ICAN, Paris, France [5]Gene Expression Laboratory, Salk Institute for Biological Studies, La Jolla, CA 92037, USA [6]ICM, Sorbonne Université, UPMC-Paris 6, UMR S 1127 / INSERM U 1127 / CNRS UMR 7225 / ICM, 75013, Paris, France [7]Department of Neurology, University of Washington, Seattle, WA 98195, USA [8]Department of Neurosurgery, University of Washington, Seattle, WA 98195, USA [9]Department of Genetics, APHP, La Pitie-Salpêtriere University Hospital, Paris, France [10]Department Cellular & Molecular Medicine, University of California, San Diego, La Jolla, CA 92093, USA [11]Department of Neurosciences, University of California, San Diego, La Jolla, CA 92093, USA [12]Howard Hughes Medical Institute, Salk Institute for Biological Studies, La Jolla, CA 92037, USA [13]Division of Biological Sciences, University of California, San Diego, La Jolla, CA 92093, USA [14]Department of Neurobiology, Duke University School of Medicine, Durham, NC 27710, USA [15]Department of Cell Biology, Duke University School of Medicine, Durham, NC 27710, USA [16]Duke Center for Neurodegeneration & Neurotherapeutics, Duke University School of Medicine, Durham, NC 27710, USA [17]Lead Contact

SUMMARY

Spinocerebellar ataxia type 7 (SCA7) is a retinal-cerebellar degenerative disorder caused by CAG-polyglutamine (polyQ) repeat expansions in the ataxin-7 gene. As many SCA7 clinical phenotypes occur in mitochondrial disorders, and magnetic resonance spectroscopy of patients revealed

*Correspondence: al.laspada@duke.edu.

AUTHOR CONTRIBUTIONS

A.R.L. provided the conceptual framework for the study. J.M.W., C.A.S., P.M.S., I.A., W.F., B.C., C.E.W., R.S.M., A.D., A.R.M., R.M.E., F.M., and A.R.L. designed the experiments. J.M.W., C.A.S., P.M.S., I.A., F.I., W.F., C., C.E.W., C.N., B.L.S., C.K., R.S.M., and A.R.L. performed the experiments. J.M.W., F.M., and A.R.L. wrote the manuscript.

SUPPLEMENTAL INFORMATION

Supplemental Information includes seven figures and two tables and can be found with this article online at https://doi.org/10.1016/j.celrep.2019.01.028.

DECLARATION OF INTERESTS

The authors declare no competing interests.

altered energy metabolism, we considered a role for mitochondrial dysfunction. Studies of SCA7 mice uncovered marked impairments in oxygen consumption and respiratory exchange. When we examined cerebellar Purkinje cells in mice, we observed mitochondrial network abnormalities, with enlarged mitochondria upon ultrastructural analysis. We developed stem cell models from patients and created stem cell knockout rescue systems, documenting mitochondrial morphology defects, impaired oxidative metabolism, and reduced expression of nicotinamide adenine dinucleotide (NAD^+) production enzymes in SCA7 models. We observed NAD^+ reductions in mitochondria of SCA7 patient NPCs using ratiometric fluorescent sensors and documented alterations in tryptophan-kynurenine metabolism in patients. Our results indicate that mitochondrial dysfunction, stemming from decreased NAD^+, is a defining feature of SCA7.

Graphical Abstract

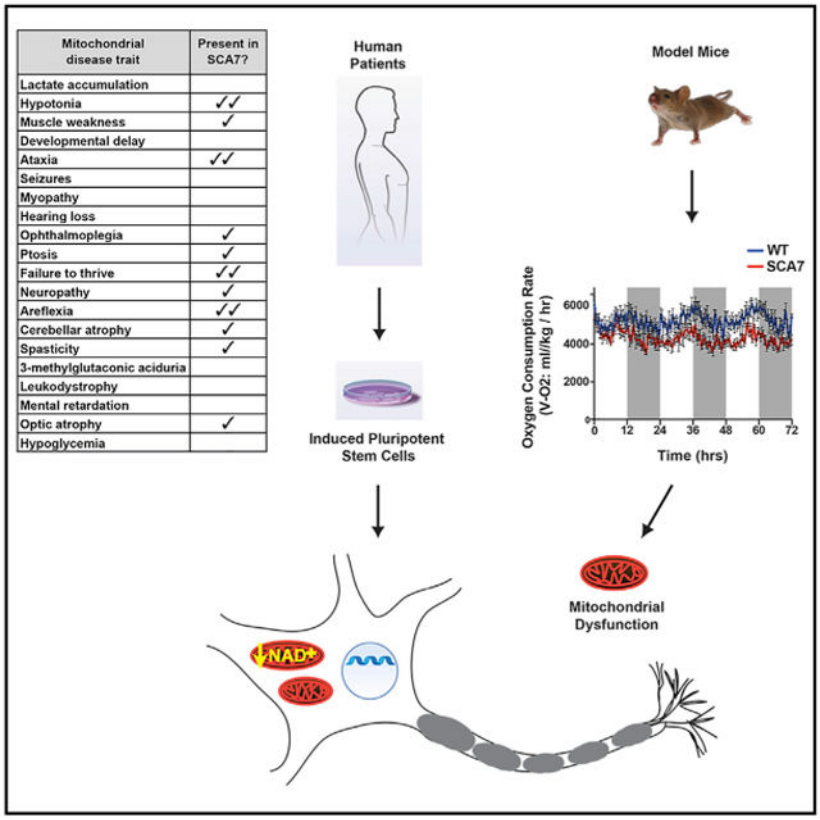

In Brief

Ward et al. document altered metabolism and mitochondrial dysfunction in SCA7 patients, mice, and human stem cell-derived neurons. They link these abnormalities to reduced nicotinamide adenine dinucleotide in specific subcellular compartments. Given the role of mitochondrial impairment in neurodegeneration, their results have therapeutic implications for SCA7 and related neurological disorders.

INTRODUCTION

Spinocerebellar ataxia type 7 (SCA7) is an inherited neurological disorder characterized by cerebellar and retinal degeneration (Garden and La Spada, 2008). SCA7 patients develop atrophy of the cerebellar cortex and the brainstem and exhibit extensive loss of cerebellar Purkinje cells (Martin et al., 1994; Michalik et al., 2004). An important feature of SCA7 that allows it to be distinguished from the more than 30 other SCAs, is retinal degeneration. Full-field electroretinograms of SCA7 patients reveal marked dysfunction of cone photoreceptor cells prior to rod photoreceptor abnormalities, establishing SCA7 as a cone-rod dystrophy (To et al., 1993). As retinal disease progresses, rod photoreceptors become involved, and the visual impairment proceeds to complete blindness. SCA7 is a degenerative disorder with a broad phenotypic spectrum: some SCA7 patients present as children and succumb to disease in less than a decade, whereas other patients remain undiagnosed until middle age and display a slowly progressive course. SCA7 is caused by a CAG/polyglutamine (polyQ) repeat expansion in the gene encoding ataxin-7; the polyQ tract ranges in size from 4 to 35 glutamines in normal subjects but expands to 37 to >300 glutamines in affected patients (David et al., 1997; Stevanin et al., 2000). There are nine recognized polyQ repeat diseases, including spinobulbar muscular atrophy (SBMA), Huntington's disease (HD), dentatorubral-pallidoluysian atrophy (DRPLA), and six forms of SCA (SCA 1, 2, 3, 6, 7, and 17). Numerous studies have shown that the initiating event in disease pathogenesis is misfolding of the polyQ expansion tract to an altered conformation that is resistant to protein degradation (Paulson et al., 2000; Ross, 1997), indicating that SCA7 shares a common pathogenic basis with Alzheimer's disease (AD), Parkinson's disease (PD), amyotrophic lateral sclerosis, and tauopathy.

Mitochondria are cellular organelles that are principally responsible for the production of cellular energy in the form of ATP and are the only organelle, other than the nucleus, containing their own DNA. Although the mitochondrial genome encodes fewer than 40 genes, many of these mitochondrial gene products are crucial for proper functioning of the oxidative phosphorylation pathway, where chemical energy is used to power ATP production. Defects in the mtDNA affecting the five multi-protein complexes of the respiratory chain cause a number of different disease syndromes (reviewed in DiMauro and Schon, 2003). These so-called mitochondrial respiratory chain disorders are quite variable in their phenotypes because of the unique features of mitochondrial genome inheritance and propagation within cells. However, despite the phenotypic variability, one recurrent theme in mitochondrial disease is the propensity for involvement of the CNS and skeletal muscle, tissues that constantly demand high levels of energy for their function. For mitochondrial diseases exhibiting CNS involvement, ataxia due to cerebellar degeneration is a common feature, with one particular syndrome known as NARP (neuropathy, ataxia, and retinitis pigmentosa) repeatedly occurring in patients who display a combination of neuropathy, ataxia, and retinal degeneration.

As mitochondrial dysfunction in mitochondrial genetic disease can often produce ataxia and retinal degeneration, which are defining features of SCA7, and nuclear genetic defects can cause various inherited ataxias with phenotypic overlap with SCA7, we hypothesized a potential role for mitochondrial dysfunction in SCA7. In infantile-onset SCA7, which is

typically caused by repeat expansions of more than 180 CAGs, progression is very rapid and patients present with a much broader spectrum of clinical phenotypes than the adult version of the disease, showing hypotonia, muscle wasting, developmental delay, and congestive heart failure (Whitney et al. (2007). Such infantile-onset SCA7 patients succumb to multi-organ failure (Ansorge et al., 2004; van de Warrenburg et al., 2001; Whitney et al., 2007). Given the multi-system and severe nature of infantile-onset SCA7, most patients undergo a diagnostic odyssey, with the work-up focused on ruling out lipid storage diseases and mitochondrial disorders (Garden et al., 1993; van de Warrenburg et al., 2001). Even the adult form of SCA7 can phenocopy mitochondrial encephalopathies, as these diseases affect similar cell types (Garden et al., 1993). Apart from a limited number of case reports, which did reveal abnormal mitochondria in SCA7 patient skeletal muscle and liver (Cooles et al., 1988; Forsgren et al., 1996; Han et al., 2010; Modi, 2000), a thorough investigation of mitochondrial involvement in SCA7 has not yet been pursued.

Here we evaluated the potential role of mitochondrial dysfunction in SCA7 through careful study of metabolic and mitochondrial function in SCA7 patients and in SCA7 mice that recapitulate childhood-onset disease (Yoo et al., 2003). Independent lines of investigation revealed compelling evidence for impaired energy metabolism and abnormal mitochondrial function. Indeed, SCA7 patients displayed impaired brain energy metabolism, and SCA7 mice exhibited decreased oxygen consumption and respiration in metabolic cage studies. In degenerating cerebellar Purkinje cells, we documented abnormal mitochondrial network size, and upon ultrastructural analysis, we observed enlarged individual mitochondria. We created induced pluripotent stem cells (iPSCs) from SCA7 patients and related controls and also developed isogenic cell lines transduced with either normal or polyQ-expanded ataxin-7. Biochemical studies of neural progenitor cells (NPCs) expressing polyQ-expanded ataxin-7 revealed markedly impaired oxidative metabolism and reduced expression of enzymes required for salvage of nicotinamide adenine dinucleotide (NAD^+). Using recently developed ratiometric NAD^+ biosensors, we measured NAD^+ levels in nucleus, cytosol, and mitochondria, and documented significantly decreased NAD^+ in the nucleus and mitochondria of SCA7 patient NPCs. Metabolomics analysis of SCA7 patients also revealed perturbations in the tryptophan-kynurenine pathway, which provides intermediates for NAD^+ biosynthesis. Our results suggest that mitochondrial dysfunction, likely due to decreased mitochondrial NAD^+, is a defining feature of SCA7 disease pathogenesis.

RESULTS

SCA7 Shares Clinical Features with Mitochondrial Disorders

SCA7 is unique among the dominant cerebellar ataxias, as affected patients typically develop retinal degeneration and manifest numerous extra-cerebellar findings, in combination with degeneration of the cerebellum and brainstem (Martin et al., 1994; Michalik et al., 2004). Given the presence of retinal involvement and the breadth of neuropathology in SCA7, the clinical picture of SCA7 is reminiscent of disorders characterized by mitochondrial dysfunction. Indeed, many SCA7 clinical phenotypes are commonly observed in mitochondrial disorders, as 11 of the top 20 disease phenotypes seen in patients with mitochondrial diseases are prominent features of the disease course in most

SCA7 patients (Figure S1A). To directly determine if SCA7 patients display significant bioenergetics defects, we performed brain 31-phosphorus (^{31}P) magnetic resonance spectroscopy (MRS) on a series of 12 SCA7 patients (Table S1) and 13 unaffected controls, all previously recruited as part of a large study of inherited SCA (Garali et al., 2017). To quantify metabolic energy status, patients and controls carried out a visual task, consisting of a pre-task resting phase, performance of the visual task, and a post-task recovery phase, during which they were subjected to ^{31}P MRS of the visual cortex. As expected, controls exhibited a significant increase in the ratio of inorganic phosphate to phosphocreatinine (Pi/P-Cr) during performance of the visual task (Figure 1A), which reflects increased mitochondrial ATP production, the latter being obtained via an elevation in ADP and reflected by a proportional increase in Pi/P-Cr. SCA7 patients, however, did not display a significant alteration in the Pi/P-Cr ratio (Figure 1A), because of impaired mitochondrial oxidative metabolism. To further assess the likelihood that SCA7 is a mitochondrial disorder, we used unbiased hierarchical clustering of SCA7 clinical features with disease phenotypes of known mitochondrial disorders using a bioinformatics algorithm (http://www.mitodb.com) (Scheibye-Knudsen et al., 2013). This analysis yielded a “mito-score” for SCA7 of 93 on a scale of 0–100; as a mito-score >50 indicates significant overlap with mitochondrial disease (Scheibye-Knudsen et al., 2013), this analysis placed SCA7 in association with a number of bona fide mitochondrial disorders, including 3-methylglutaconic aciduria type III (MGCA3) and two forms of optic atrophy (Figure S1B). Hence, both ^{31}P MRS evaluation of SCA7 patients and consideration of SCA7 clinical symptomatology provide compelling evidence for mitochondrial dysfunction as a central feature of the SCA7 disease process.

SCA7 Mice Exhibit Abnormal Metabolism

As oxidative metabolism occurs in mitochondria, we initiated our assessment of mitochondrial function in SCA7 by examining metabolic physiology in the SCA7 266Q knockin mouse model, as these SCA7 mice recapitulate a rapidly progressive juvenile-onset form of disease (Yoo et al., 2003). To quantify metabolic function in living mice, we used the Oxymax/Comprehensive Lab Animal Monitoring (CLAMS) cage system to determine the oxygen consumption rate (OCR) and the respiratory exchange rate (RER) for symptomatic SCA7 266Q knockin mice and wild-type littermate controls. We found that SCA7 mice consumed significantly less oxygen overall with no difference for time of day (Figures 1B and 1C). We also measured RER and observed a significant decrease in RER in SCA7 mice (Figures 1D and 1E), suggesting reduced reliance on glucose oxidation. Taken together, these findings indicate that metabolic function is impaired in SCA7.

Altered Adipose Tissue Stores and Blood Glucose Levels in SCA7 Mice

To further characterize the nature of the abnormal metabolism detected in SCA7 266Q knockin mice, we evaluated their adipose tissue and found that SCA7 fat depots are visibly smaller in comparison with littermate controls (Figure 2A). Analysis of inguinal white adipose tissue (iWAT) revealed that SCA7 mice and littermate controls possess iWAT depots that are comparable as a fraction of total body weight at disease onset, but with disease progression, SCA7 mice display a rapid decrease in iWAT volume in proportion to total body weight, which worsens with disease course (Figure 2B). This dramatic loss of adipose

tissue occurs despite the fact that food consumption by SCA7 mice and littermate controls was comparable (Figure 2C) but was accompanied by a significant drop in body weight in SCA7 mice (Figure S2A). We also assessed fasting blood glucose levels and found that SCA7 mice and littermate controls display similar blood glucose levels at disease onset, but SCA7 mice exhibit markedly reduced blood glucose levels, once visibly affected with significant neurological abnormalities (Figures 2D, S2B, and S2C) but prior to late-stage disease (Figure S2D). Decreases in adipose tissue content and blood glucose levels imply an abnormal regulation of energy metabolism in symptomatic SCA7 mice. Coupled with the results of metabolic cage experiments, these findings confirm that metabolic respiration is compromised in symptomatic SCA7 mice.

SCA7 Cerebellar Purkinje Cells Have a Fragmented Mitochondrial Network Consisting of Enlarged Individual Mitochondria

Purkinje cells in the cerebellum are among the most metabolically active of all neurons (Howarth et al., 2010), as they process an enormous amount of information from the brainstem and deep cerebellar nuclei to provide the only efferent output leaving the cerebellar cortex for regulation of voluntary movement. In SCA7, Purkinje cell degeneration is prominent; hence, we immunostained cerebellar sections from SCA7 266Q knockin mice and littermate controls with an antibody directed against the outer mitochondrial membrane protein Tom20. We then skeletonized and quantified the Tom20 immunopositive signal to evaluate mitochondrial content and morphology in the soma of Purkinje cells (Figure 2E). By quantifying Tom20 fluorescence as a function of overall cell size, we determined the mitochondrial area and observed a marked reduction in mitochondrial area in SCA7 mice (Figure 2F). When we measured the length of the mitochondrial network in Purkinje cells, we documented a significant reduction in average mitochondrial network length in SCA7 mice in comparison with littermate controls (Figure 2G). A decrease in mitochondrial network length is consistent with a more fragmented mitochondrial network, which has been associated with decreased respiration and defective bioenergetics (Knott et al., 2008; Westermann, 2012). To further characterize the morphology of mitochondria at the single organelle level, we pursued ultra-structural analysis on ultrathin sections of cerebellum from SCA7 and control mice. Inspection of the resultant electron micrographs revealed that individual mitochondria in SCA7 mice are obviously larger in both the soma and dendrites of cerebellar Purkinje cells (Figures 3A and 3B). To quantify this apparent difference, we measured the area, perimeter, and feret diameter of individual mitochondria from SCA7 mice and littermate controls and documented that individual mitochondria in SCA7 cerebellar Purkinje cells are much larger in size than mitochondria in control Purkinje cells for all of these readouts (Figures 3C–3H). We also evaluated mitochondrial morphology by assessing circularity and aspect ratio and found that despite the increase in size, mitochondria in SCA7 cerebellar Purkinje cells are similar in shape to mitochondria in control Purkinje cells (Figures S3A–S3D), and mitochondrial protein content in SCA7 and control cerebellum is similar (Figures S3E and S3F). To assess the status of mitochondria in peripheral tissues, we immunostained skeletal muscle sections from SCA7 266Q knockin mice and littermate controls and noted marked increases in mitochondrial content, size, and network length in SCA7 skeletal muscle, which was accompanied by significant increases in the protein expression levels of Drp1 and Mfn1 (Figure S4). We also analyzed liver sections

from SCA7 266Q knockin mice and matched controls, and although we noted significantly increased Tom20 immunofluorescence and mitochondrial network length, mitochondrial area and mitochondria-associated protein expression levels were comparable (Figure S5).

Development, Comparison, and Validation of Different SCA7 Human Stem Cell Models

To determine if the metabolic and mitochondrial defects in SCA7 mice occur in SCA7 patients, we derived iPSCs from SCA7 patients and their related, unaffected relatives (Figure S6A) using retroviral transduction (Takahashi and Yamanaka, 2006). Prior to the use of iPSCs and their derivatives, we confirmed their identity, pluripotency, and ploidy. After generating NPCs, we examined mitochondrial network length via Tom20 immuno-staining and noted a marked reduction in mitochondrial network length in the most severely affected SCA7 patient with a CAG-70 (70Q) repeat expansion mutation but observed only modest decreases in SCA7 patients with CAG-50 (50Q) and CAG-65 (65Q) repeat expansion mutations (Figure 4A). We completed a battery of other assays and did not detect disease-specific phenotypes, despite using multiple clones per genotype. As prior modeling efforts in the CAG-polyQ disease field have shown that greatly expanded CAG repeat alleles are often necessary to elicit disease-specific phenotypes, and stem cell modeling using lines of identical genetic background can greatly reduce spurious effects, we derived a SCA7 stem cell model system that would permit direct comparison of ataxin-7-113Q and normal ataxin-7. To achieve this, we used CRISPR/Cas9 genome editing to first knock out the *ATXN7* gene in patient iPSCs with a guide RNA proximal to the CAG repeats, ensured its efficiency in a surveyor nuclease assay (Figure S6B), verified indels in each *ATXN7* allele, and finally confirmed absence of ataxin-7 protein expression (Figure S6C). We then reintroduced expression of either normal length ataxin-7-10Q or polyQ-expanded ataxin-7-113Q with eGFP separated by a 2A peptide, or empty vector-eGFP for control purposes, each carried on a lentiviral vector (Figure 4B). The decision to derive vector only, ataxin-7-10Q, and ataxin-7-113Q isogenic iPSC lines reflects the technical challenges encountered with precise genome editing of repetitive sequence contained on a homology stretch that spans the repeat region. Nonetheless, this knockout rescue system permits direct comparison of lines that differ only in the expression of the polyQ expansion tract within the ataxin-7 protein, as we confirmed equivalent levels of expression of ataxin-7-10Q and ataxin-7-113Q protein in the iPSC derivatives and continued to monitor expression levels in all subsequent studies. Indeed, when we compared our SCA7 patient-derived NPCs with our SCA7 knockout rescue NPCs, we found that accumulation of aggregated ataxin-7 protein was similar between SCA7 10Q, 65Q, and 70Q NPCs upon filter trap assay (Figure 4C), while only ataxin-7-113Q NPCs exhibited marked accumulation of aggregated ataxin-7 protein upon filter trap analysis (Figure 4D). The existence of polyQ length-dependent disease phenotypes in this “SCA7 knockout rescue system” was also evident when we studied cell toxicity, as only the SCA7 65Q NPC line displayed significant levels of cell death, with both SCA7 50Q and SCA7 70Q NPCs showing cell death levels comparable with control SCA7 10Q NPCs (Figure 4E); however, we documented markedly increased cell death in ataxin-7-113Q NPCs in comparison with non-transduced NPCs, eGFP-only expressing NPCs, and ataxin-7-10Q NPCs (Figure 4F). These studies thus validate the utility of the SCA7 knockout rescue NPC model as a system for further study of SCA7 metabolic and mitochondrial disease phenotypes.

Polyglutamine-Expanded Ataxin-7 Yields Mitochondrial Abnormalities and Bioenergetics Defects in Transduced NPCs

To determine if expression of polyQ-expanded ataxin-7 elicits metabolic and mitochondrial phenotypes in human stem cell-derived NPCs, we immunostained knockout rescue NPCs expressing either GFP only, ataxin-7-10Q, or ataxin-7-113Q with an antibody directed against Tom20 (Figure 5A), compared mitochondrial network length, and documented a marked, polyQ length-dependent reduction in mitochondrial network length (Figure 5B). To functionally assess mitochondrial respiration, we performed a bioenergetics profile of non-transduced, GFP-only, ataxin-7-10Q, and ataxin-7-113Q NPCs by performing extracellular flux analysis. We found that ataxin-7-113Q-expressing NPCs display a markedly reduced OCR and greatly increased extracellular acidification rate (ECAR) at baseline to yield a dramatically low OCR/ECAR ratio compared with non-transduced, GFP-only, and ataxin-7-10Q NPCs (Figure 5C). This diminished OCR/ECAR ratio persists in ataxin-7-113Q NPCs upon treatment with the ATP synthase inhibitor oligomycin, the uncoupling agent FCCP, and complex I + III inhibition with combined antimycin and rotenone treatment (Figure 5C).

Biosensor Quantification Reveals Reduced NAD^+ in Specific Subcellular Compartments in SCA7 Patient NPCs

One possible explanation for impaired oxidative metabolism in SCA7 could be diminished NAD^+, as NAD^+ provides substrate for production of NADH, the key electron donor in production of a chemiosmotic gradient that drives oxidative phosphorylation at the inner mitochondrial membrane, and microarray expression analysis of SCA7 266Q knockin mice had previously revealed a significant reduction in the expression of NMNAT1 (Gatchel et al., 2008), which catalyzes synthesis of NAD^+ from nicotinamide mononucleoside (NMN) in the salvage pathway. The vast majority of NAD^+ is generated via addition of AMP to NMN in the salvage pathway; however, as NAD^+ is abundantly required in different subcellular compartments, mammalian cells possess three distinct NMN adenylyltransferases in these different compartments: nuclear NMNAT1, cytosolic NMNAT2, and mitochondrial NMNAT3 (Revollo et al., 2004). To broadly evaluate NMNAT enzyme expression in SCA7, we performed qRT-PCR analysis of NMNAT1, NMNAT2, and NMNAT3 on RNAs obtained from GFP-only, ataxin-7-10Q, and ataxin-7-113Q NPCs and observed marked reductions in NMNAT1, NMNAT2, and NMNAT3 gene expression in ataxin-7-113Q NPCs, though reductions in NMNAT2 and NMNAT3 were also observed in ataxin-7-10Q NPCs (Figures 6A–6C). We similarly evaluated Sirt3 and Sirt6, two sirtuin family members with links to NAD^+ metabolism, and documented reductions in Sirt3 expression in ataxin-7-10Q and ataxin-7-113Q NPCs but noted comparable expression levels of Sirt6 (Figures S6D and S6E). Immunoblot analysis revealed a reduction in NMNAT1 protein expression in ataxin-7-113Q NPCs but indicated a similar reduction in NMNAT1 protein expression in ataxin-7-10Q NPCs (Figure 6D). Although these findings imply that NAD^+ production may be impaired in SCA7, they do not provide direct evidence for altered NAD^+ metabolism in SCA7. Hence, to accurately quantify NAD^+ levels and do so at the subcellular level, we turned to a recently developed set of NAD^+ biosensors. In this ratiometric system, NAD^+ binding yields a loss of fluorescence at an excitation wavelength of 488 nm but does not affect a second excitation peak at 405 nm, permitting normalization (Cambronne et al.,

2016). In the presence of reduced NAD^+, one would expect increases in relative F_{488}/F_{405} fluorescence, which we validated in all three NAD^+ biosensors by measuring a respective increase in the F_{488}/F_{405} fluorescence in the nucleus, cytosol, and mitochondria of HeLa cells treated with the NAD^+ depleting drug FK866 (Figure S6F). We then resorted to the use of patient NPC lines, as the knockout rescue system is incompatible with the biosensors because of the presence of GFP. When we compared NAD^+ levels in control and SCA7 NPCs, we documented a significant decrease in NAD^+ levels, as reflected by an increase in the 488/405 fluorescence ratio, in the nucleus and mitochondria of SCA7 NPCs (Figure 6E). There was also a strong trend toward reduced cytosolic NAD^+ levels in SCA7 NPCs, but this difference was not statistically significant ($p = 0.09$). These findings indicate that metabolic and mitochondrial dysfunction in SCA7 may result from reduced NAD^+ availability in certain subcellular compartments.

Metabolomics Analysis of SCA7 Patients Reveals Perturbations in the Tryptophan-Kynurenine Pathway

Besides the salvage pathway that recycles nicotinamide to produce NAD^+, there is a *de novo* pathway for NAD^+ synthesis in which tryptophan is converted to kynurenine and then ultimately to quinolinate, which is a key precursor to NAD^+ (Figure S7). To further assess the status of NAD^+ production in SCA7, we performed metabolomics analysis on plasma samples from 13 fasted SCA7 patients (Table S1) and 35 fasted controls, as part of a larger biomarker study in SCA patients (Garali et al., 2017). Using high-resolution mass spectrometry coupled to liquid chromatography (LC-HRMS), we detected and quantified tryptophan and related metabolites from the tryptophan-kynurenine pathway (Table S2). Although tryptophan, kynurenine, and the kynurenine/tryptophan ratio were comparable in SCA7 patients and controls (Figures 7A–7C), we observed a trend toward increased levels of 5-hydroxytryptophan in SCA7 patient plasma samples (Figure 7D), indicating reduced flux to the NAD^+ precursor quinolinate. Furthermore, we found that kynurenic acid and xanthurenic acid were significantly increased in plasma samples of SCA7 patients compared with controls (Figures 7E–7F). Increased production of kynurenic acid and xanthurenic acid in SCA7 patients likely reflects increased activity of kynurenine aminotransferase (KAT), which would hamper the synthesis of the quinolinate precursor and therefore NAD^+ (Figure S7). Interestingly, the same metabolomics analysis was performed on patients with SCA1, SCA2, and SCA3, but such alterations in the tryptophan- kynurenine pathway were not present in these SCA patients (data not shown). These results indicate that tryptophan metabolism and the formation of NAD^+ intermediates are specifically altered in SCA7 patients and thus corroborate our findings of reduced NAD^+ levels in human stem cell models of SCA7.

DISCUSSION

Mitochondrial dysfunction is emerging as a unifying feature of many neurodegenerative disorders, including AD, PD, and HD (Filosto et al., 2011; Golpich et al., 2017; Lin and Beal, 2006). Despite the importance of mitochondrial function for CNS regions that are selectively vulnerable in SCA7, mitochondrial dysfunction in SCA7 has not yet been carefully examined. To determine the role of mitochondrial dysfunction in SCA7 patients,

we performed ^{31}P MRS of the visual cortex and documented direct evidence for impaired mitochondrial oxidation, on the basis of the inability of SCA7 patients to increase ATP production during completion of a visual task. Changes in the Pi/P-Cr ratio have been linked to altered mitochondrial oxidative metabolism (Chance et al., 1981; Wiener et al., 1986), and previous MRS analysis of patients with HD, a polyQ repeat disease associated with mitochondrial energy deficiency, similarly revealed no change in the Pi/P-Cr ratio during visual stimulation (Adanyeguh et al., 2015; Mochel et al., 2012). Importantly, such brain metabolic alterations could be corrected when HD patients were treated with triheptanoin, a drug that directs key substrates to the Krebs cycle (Adanyeguh et al., 2015). In addition to evaluating mitochondrial dysfunction in SCA7 patients, we pursued an in-depth analysis of the metabolic physiology of SCA7 266Q knockin mice (Yoo et al., 2003), which recapitulate juvenile-onset disease. Metabolic cages were used to derive accurate measures of OCR and RER and revealed significant deficits in both OCR and RER in SCA7 mice. Similar studies of metabolic physiology have been completed for one other related polyQ disorder, HD, and revealed no differences in basal metabolic rate in one case and an increase in OCR in the other case (Hamilton et al., 2015; Weydt et al., 2006). Our detection of decreased OCR and RER in SCA7 mice thus provides evidence for physiologically relevant decreases in metabolic processes in a polyQ repeat disease.

After performing *in vivo* metabolic studies, we considered the morphology of the mitochondrial network and of individual mitochondria in cerebellar neurons in SCA7 mice, as bioenergetics defects can reflect abnormalities in mitochondrial dynamics (Knott et al., 2008; Mishra and Chan, 2016). We observed fragmentation of the mitochondrial network in SCA7 cerebellar Purkinje cells, suggesting that the integrity of the mitochondrial network was not being maintained properly, likely because of defective mitochondrial dynamics. Ultrastructural analysis, however, clearly revealed that individual mitochondria in SCA7 cerebellar Purkinje cells are significantly enlarged not just in Purkinje cell soma but also in dendrites. Although a fragmented mitochondrial network often occurs when individual mitochondria are reduced in size, the relationship between the size of the overall mitochondrial network at micron scale and the size of individual mitochondria at nanoscale is not always absolute (Rafelski, 2013). Indeed, yeast mutants, which lack normal mitochondrial fusion or fission and thus possess abnormally small or abnormally large individual mitochondria, can nonetheless maintain a mitochondrial network of normal size (Sesaki and Jensen, 1999). Purkinje cells are exquisitely sensitive to mitochondrial morphology defects, because if mitochondria are too large, they cannot enter the narrow neuronal projections of their elaborate dendritic network (Narendra and Youle, 2012). The presence of functioning mitochondria in Purkinje cell dendrites is essential, as Purkinje cells are highly electrically active and thus continually pumping ions across the synapses located in their dendrites, processes that require quick access to large quantities of ATP (Howarth et al., 2010). Studies of other cerebellar ataxias, such as autosomal recessive spastic ataxia of Charlevoix-Saguenay (ARSACS), confirm the importance of mitochondrial size regulation for proper Purkinje cell function, as loss-of-function of sacsin in knockout mice yielded abnormally enlarged mitochondria, which were precluded from entering the narrow neuronal projections of Purkinje cell dendrites, resulting in Purkinje cell degeneration (Girard et al., 2012). Similarly in mice, neuron-specific loss of function of Drp1, a key regulator of

mitochondrial fission, yields abnormally enlarged mitochondria and severe Purkinje cell degeneration, with a paucity of mitochondria found in Purkinje cell dendrites (Narendra and Youle, 2012). Detection of abnormally enlarged individual mitochondria in SCA7 cerebellar Purkinje cells suggests that mitochondrial abnormalities likely play a central role in promoting degeneration of this crucial neuron subtype. Interestingly, despite the presence of a fragmented mitochondrial network in cerebellar neurons in SCA7 mice, we found that the mitochondrial network is actually increased in the skeletal muscle and liver of SCA7 266Q knockin mice, with evidence for increased mitochondrial protein content in skeletal muscle. These findings are consistent with previous studies that reported mitochondrial abnormalities in liver and skeletal muscle biopsies from SCA7 patients (Cooles et al., 1988; Forsgren et al., 1996; Han et al., 2010; Modi, 2000).

Although mouse models of SCA7, and of other polyQ repeat diseases, recapitulate many of the defining clinical features of these disorders, there has been great interest in producing neural cells from affected patients by reprogramming terminally differentiated fibroblasts into iPSCs. Here we derived iPSCs from two different SCA7 pedigrees to permit comparison of affected patients with their genetically related unaffected relatives. Despite taking this approach, which should reduce variability because we are comparing individuals with closely related genomes, we did not observe consistent phenotype differences between SCA7 patients and unaffected controls. To create a more powerful stem cell model for SCA7, we used genome editing with CRISPR-Cas9 in order to produce isogenic lines that would differ only in expression of mutant ataxin-7 protein. Although contraction of the CAG repeat expansion to an inframe, normal-sized repeat was not achieved because of the challenges of homologous recombination with targeting fragments containing repetitive sequences, we did produce cell lines with complete knockout of ataxin-7 and transduced one such validated cell line with lentivirus constructs expressing normal ataxin-7, polyQ-expanded ataxin-7, or nothing (i.e., empty vector). We confirmed comparable expression of ataxin-7 by immunoblot analysis of transduced iPSCs and their NPC derivatives and then evaluated mitochondrial network size and metabolic function, after demonstrating that expression of polyQ-expanded ataxin-7 yielded disease-relevant phenotypes in comparison with NPCs expressing normal ataxin-7 or no ataxin-7. We detected fragmentation of the mitochondrial network in the ataxin-7-113Q NPCs and documented marked impairment in mitochondrial bioenergetics by extracellular flux analysis. These findings corroborated observed phenotypes in SCA7 mice, independently validating the existence of mitochondrial dysfunction in SCA7. As this analysis included evaluation of human neural cells lacking ataxin-7, our results indicate that loss of function of ataxin-7 is well tolerated, as non-transduced and GFP-empty transduced ataxin-7 knockout NPCs exhibited mitochondrial networks and bioenergetics comparable with ataxin-7-10Q NPCs. With the potential application of dosage reduction therapies such as antisense oligonucleotides or RNAi for SCA7 and related polyQ ataxias (Ramachandran et al., 2014, 2016; Scoles et al., 2017), absence of deleterious phenotypes in human ataxin-7 knockout neural derivatives is encouraging, because non-allele-selective interventions are currently envisioned.

So what then is the mechanistic basis for mitochondrial dysfunction in SCA7? The co-existence of bioenergetics defects with aberrant mitochondrial morphology does not allow us to distinguish between defective mitochondrial dynamics or impaired metabolism as the

initiating event in the pathogenic cascade, though they are not mutually exclusive. Ataxin-7 is a transcription factor core component of the STAGA co-activator complex (Helmlinger et al., 2004; Palhan et al., 2005), and we, and others, have reported that transcription dysregulation contributes to SCA7 disease pathogenesis (La Spada et al., 2001; Yoo et al., 2003). When we considered the results of microarray expression analysis of the SCA7 mouse model used in this study, we noted a marked reduction in the expression of the gene encoding NMNAT1 in SCA7 266Q cerebellum (Yoo et al., 2003). NMNAT1 is required for generation of NAD^+ by the recycling of nicotinamide via the salvage pathway, which is the principal pathway by which NAD^+ levels are maintained. NAD^+ is emerging as an important regulator of cellular function, and its depletion has been linked to a number of neurodegenerative disorders (Long et al., 2015; Ryu et al., 2016; Wang et al., 2016; Williams et al., 2017). Although NMNAT1 is found in the nucleus, and NMNAT2 and NMNAT3 operate respectively in the cytosol and mitochondria, previous work has shown that NAD^+ levels in one compartment can affect NAD^+ levels in other compartments (Rustin et al., 1996), indicating that reduced NAD^+ production in the nucleus could affect mitochondrial NAD^+ availability, which in turn would decrease levels of NADH, the electron donor that drives oxidative metabolism at the inner mitochondrial membrane. Furthermore, reduced NAD^+ in the nucleus alone is sufficient to impair mitochondrial oxidative phosphorylation, as NAD^+ is the required co-factor for Sirt1, which deacetylates PGC-1α to activate it (Rodgers et al., 2005). PGC-1α co-activates the expression of genes that promote mitochondrial biogenesis or encode many of the enzymes required for both Krebs cycle and oxidative phosphorylation pathway function (Kelly and Scarpulla, 2004).

In light of the importance of NAD^+ production for mitochondrial bioenergetics, we measured the expression of NMNAT1, NMNAT2, and NMNAT3 in our SCA7 knockout rescue stem cell model and noted a marked reduction in NMNAT1 gene expression in ataxin-7-113Q expressing NPCs in comparison with ataxin-7-10Q expressing NPCs. For NMNAT2 and NMNAT3, however, marked reductions were documented in both ataxin-7-113Q and ataxin-7-10Q expressing NPCs, and NMNAT1 immunoblot analysis revealed similar reductions in NMNAT protein expression in ataxin-7-113Q and ataxin-7-10Q expressing NPCs. These findings indicate that altered NAD^+ production could be occurring in SCA7, but these results were not definitive. To directly measure NAD^+ levels, and do so in the different subcellular compartments where NMNAT1, NMNAT2, and NMNAT3 function, we used a set of recently developed ratiometric fluorescent biosensors (Cambronne et al., 2016). Using this technique, we determined that NAD^+ levels are significantly reduced in the nucleus and mitochondria of ataxin-7-113Q-expressing NPCs in comparison with ataxin-7-10Q-expressing NPCs, with a trend toward a significant reduction noted in the cytosol of ataxin-7-113Q NPCs. Direct measurement of NAD^+ levels in subcellular compartments in SCA7 thus provides evidence for reduced NAD^+ in mitochondria as a key contributor to the impaired mitochondrial oxidation detected in SCA7 mice and patients. Indeed, previous work indicates that mitochondria NAD^+ levels are regulated separately from nuclear or cytosolic NAD^+, because knockdown of NMNAT3 yielded a marked decrease in mitochondrial NAD^+ without affecting nuclear or cytosolic NAD^+ levels (Cambronne et al., 2016). In addition to the salvage pathway that recycles nicotinamide to generate NAD^+, metabolism of tryptophan to kynurenine and then to

quinolinate provides a key substrate precursor for *de novo* synthesis of NAD^+. To determine if altered tryptophan metabolism is also contributing to the shortage of NAD^+ in SCA7, we performed metabolomics analysis on SCA7 patients and documented marked increases in kynurenic acid and xanthurenic acid, which suggests a metabolic detour to the detriment of quinolinate formation and therefore NAD^+ synthesis. Hence, we propose that reduced mitochondrial NAD^+ in SCA7 is contributing to the mitochondrial dysfunction observed in this disorder. As numerous efforts are under way to achieve NAD^+ repletion as a treatment for age-related diseases, including neurodegenerative disorders (Guarente, 2016), our results may have therapeutic implications for SCA7 and also for other related neurodegenerative diseases, in which mitochondrial involvement is likely.

STAR★METHODS

CONTACT FOR REAGENT AND RESOURCE SHARING

Further information and requests for resources and reagents should be directed to and will be fulfilled by the Lead Contact, Albert La Spada (al.laspada@duke.edu).

EXPERIMENTAL MODEL AND SUBJECT DETAILS

Cell Lines—Fibroblasts were generated from dermal biopsies from SCA7 patients and controls, upon informed consent and in compliance with UCSD and Duke IRB protocols. Age, genotype, and sex of each resultant cell line is defined in Figure S6A. Low passage fibroblast cultures were treated with the retroviral reprogramming factors Oct4, Sox2, Klf4, and c-Myc, as described previously (Takahashi et al., 2007). After 15-20 days, individual colonies with stem cell morphology were isolated and transferred to feeder free conditions and thereafter maintained on Matrigel (BD Bioscience) coated plates and grown in mTesr1 media (StemCell Technologies) as clonal lines. Thereafter, cells were passaged manually by cutting colonies with a needle and scraping resulting sections off the plate before transferring to a new dish. All iPSCs were maintained in 4% O_2/5% CO_2 at 37°C with daily medium changes. Characterization of resulting iPSC lines and NPC differentiation is described below in Method Details.

Animals—All animal experimentation adhered to NIH guidelines and was approved by and performed in accordance with the University of California, San Diego and Duke University Institutional Animal Care and Use Committees. The development of the SCA7 266Q mice has been previously described ((Yoo et al., 2003). SCA7 266Q animals were maintained on the FVB/NJ background and then backcrossed onto the C57BL/6J strain background. Mice were housed in a temperature- and humidity-controlled environment on a 12-hour light/dark cycle with food and water *ad libitum*. Hemizygous and age-matched wild-type littermates were used for all experiments. Ages and sample sizes are indicated in each associated figure legend. Because of challenges with breeding the SCA7 266Q line, only female mice were used in metabolic experimentation and quantification of fat percentage, food intake, and glucose levels. For microscopy experimentation, females and males were used in equal numbers, or as close to equal numbers as possible, and studies were performed by an examiner blinded to the treatment.

Human subject studies—The patient study (NCT 01470729) was sponsored by the Assistance-Publique des Hôpitaux de Paris and approved by the local ethical committee (AOM10094, CPP Ile de France VI, Ref: 105-10). All participants were over 18 years and signed a written informed consent before they participated in the study. The patient group consisted of 6 men and 6 women aged from 22 to 76 years old. Sample sizes are indicated in each associated figure legend.

METHOD DETAILS

31-Phosphorus functional magnetic resonance spectroscopy (^{31}P-MRS)—^{31}P-MRS data were acquired on a 3-Tesla whole-body Siemens Magnetom Trio scanner, as previously described (Adanyeguh et al., 2015; Mochel et al., 2012). A6-cm^{31}P transmit/receive surface coil (RAPID Biomedical GmbH; Rimpar, Germany) was used to collect free induction decays at the three phases from the visual cortex of 12 SCA7 patients and 13 healthy controls. The ratio of inorganic phosphate (Pi) to PCr (Pi/P-Cr ratio) was calculated to evaluate the brain response to cortical activation.

Metabolomics analysis on plasma samples—Details about reagents, sample preparations, experimental settings and data-processing were as published previously (Garali et al., 2017). Metabolomics features related to tryptophan metabolism were identified based on their mass over charge ratio (*m/z*), their MS/MS spectra, and their retention times using an *in-house* database generated from available commercial standards (Garali et al., 2017).

MitoDB analysis: SCA7 was queried against the MitoDB database < http://www.mitodb.com> with incidence of 100% ataxia, 83% visual acuity, 30% visual impairment, 69% optic atrophy, 43% pigmentary retinopathy, 70% ophthalmoplegia, 50% pyramidal signs, 50% extrapyramidal symptoms, 50% spasticity, and 25% hearing loss.

Mouse phenotyping studies: For neurological dysfunction studies, mice were visually inspected by a blinded examiner for obvious neurological signs and examined using a composite neurological evaluation tool (ledge test, clasping, kyphosis and gait were scored on a scale of 0 (normal) to 3 (severely impaired)), as described previously (Guyenet et al., 2010). Females and males were used in equal numbers, or as close to equal numbers as possible, and studies were performed by a blinded examiner. For survival studies, animals were monitored daily and pronounced dead when respiration or heartbeat was no longer present.

Fluorescence microscopy: Ten-week-old mice were deeply anesthetized with isoflurane and perfused with 4% PFA. Brains were dissected, immersed in 30% sucrose, and cut on a vibrating microtome into 30 um sagittal sections. These free-floating sections were incubated in blocking solution containing 10% goat serum, 1% BSA, and 0.3% Triton X-100 for 1 hr at RT. The quadriceps muscles and livers were removed and snap-frozen in an isopentane bath cooled by liquid nitrogen and stored at −80°C until use. 5-μm cross sections were cut using a cryostat at −20°C, collected on glass slides, and dried at RT for 10 min. The sections were fixed in 1.5% PFA followed by incubation in 0.05% Triton X and subsequently blocked via incubation in 5% BSA in PBS for 1 hr at RT. Primary antibodies,

anti-Calbindin antibody (Sigma-Aldrich, C9848) and anti-Tom20 (Santa Cruz, sc11415), were diluted 1:500 in blocking solution and sections were incubated overnight at 4°C. After 2 washes with PBS, sections were incubated with anti-mouse superclonal AlexaFluor 488 and anti-rabbit AlexaFluor 555 (Fisher) at 1:500 and 1:250 dilutions, respectively, for 1 hr at RT. Sections were then washed one time in PBS, incubated in PBS supplemented with 1:5000 Hoechst 33342 for 10 min at RT, and washed again before mounting on glass slides with Prolong Gold anti-fade reagent (Life Technologies). Images were taken on a fluorescence microscope (Z1 Axio Observer Apotome or LSM 880 inverted confocal microscope with AiryScan, Zeiss). Equivalent numbers of fields were captured for each condition. Each Purkinje cell soma was manually encircled based on Calbindin staining and morphometry parameters were quantified by an ImageJ plugin, as described previously (Dickey and Strack, 2011). Mitochondrial area was calculated as a percentage of the soma area. Average mitochondrial length was quantified in microns.

Electron microscopy and mitochondrial ultrastructure: Eight and half-week-old mice were deeply anesthetized with isoflurane and perfused with a fixative solution made of 2% PFA and 2.5% glutaraldehyde in PBS. Brains were dissected and placed in fixative solution overnight at 4°C. The brains were cut on a vibrating microtome into 50 um sagittal sections. Ultrathin sections were prepared from equivalent regions within the cerebellum and imaged at 4000x on a Carl Zeiss Libra 120kV PLUS Energy Filtered Transmission Electron Microscope at the Salk Institute Biophotonics Core. Individual mitochondria were traced in ImageJ and measured for area, perimeter, feret diameter (caliper length), circularity ($4\pi A/p^2$), and aspect ratio (major axis/minor axis).

Metabolic studies Indirect calorimetry in metabolic cages: Female 8.5-week-old mice were housed in the Oxymax/CLAMS metabolic cage system from Columbus Instruments for 4 days with *ad libitum* access to food and water on a 12 hr light/dark cycle. VO2 and RER were measured by the Oxymax system after a 24 hr acclimation period.

Glucose measurement and iWAT dissection: Glucose was measured using the NovaMAX glucometer system via tail venipuncture after 6 hr of fasting. The whole mouse was weighed just prior to anesthetization, then sacrified and the inguinal white adipose tissue from the right side of each mouse was surgically excised and weighed as described previously (Lim et al., 2012). Variance in sample size between groups at different time points occurred due to increased sampling rate of both genotypes at later time points for other lines of experimentation.

RT-PCR analysis: RNA was extracted from cells using TRIzol reagent (Thermo Fisher), and DNase-treated with TURBO DNA-free kit (ThermoFisher) according to manufacturer's instructions. One microgram (ug) of RNA was reverse transcribed using the High-Capacity cDNA Reverse Transcription Kit (Applied Biosystems, Life Technologies) according to manufacturer's instructions. cDNA was then amplified using a Taqman probe against NMNAT1.

Protein isolation and immunoblotting analysis: Cells were harvested in RIPA buffer (50 mM Tris, 0.1% SDS, 0.5% sodium deoxycholate, 1% Triton X-100, 150 mM NaCl)

supplemented with 1% protease inhibitor cocktail (Roche) and homogenized by passing 5 times through a 23-gauge needle. Lysate was then centrifuged at 10000 x *g* for 10 min at 4°C. Supernatant was quantified via BCA assay (Pierce; ThermoFisher). Fifteen micrograms of protein were separated on 4%–12% Bis-Tris gels (Life Technologies), transferred to PVDF membranes (Millipore), and blocked with 3% Bovine Serum Albumin (Sigma-Aldrich) for at least 1 hr at RT. Membranes were then probed with rabbit anti-ATXN7 (Thermo, PA1-749) 1:1000, mouse anti-polyQ 1C2 (Millipore MAB1574), rabbit anti-TOMM20 (Novus NBP1-81556) 1:1000, mouse anti-MFN1 (Abcam ab57602) 1:1000, mouse anti-DRP1 (Abcam ab56788) 1:1000 or mouse anti-beta actin (Abcam, ab8226) 1:10000 in 3% BSA in PBS overnight at 4°C. After 3 washes with 1x phosphate buffered saline supplemented with 0.1% Tween20 (PBS-T), membranes were incubated with HRP secondary antibodies (1:10000 Santa Cruz sc-2005 [anti-mouse], sc-2004 [anti-rabbit]) in PBS-T for 1 hr at RT. After treatment with ECL detection reagent (Denville), the membranes were visualized by autoradiography. For the filter trap assay, 30 mg of protein was loaded in a PR-600 24 slot blot filtration manifold unit (Hoefer, Fisher Scientific) with a cellulose acetate membrane. Vacuum was applied until lysate had run through, membrane was blocked in 5% nonfat dried milk in PBS for 1 hr at RT, and then incubated in mouse anti-polyQ 1C2 (Millipore MAB1574) 1:1000 overnight at 4°C. Membranes were then incubated in anti-mouse secondary antibody (1:5000; Santa Cruz sc-2005) for 1 hr at RT, and visualized as above.

Immunohistochemistry: Cells were grown in coated 96-well plates or chamber slides, fixed in 4% paraformaldehyde for 10 min, and permeabilized in 0.3% Triton X-100 in PBS for 10 min. Cells were then blocked with 5% BSA for at least 1 hr before incubation with chicken anti-GFP (Abcam, ab13970) 1:2000, rabbit anti-Tom20 (Santa Cruz, SC11415) 1:500, mouse anti-SSEA4 (Cell Signaling CS 4755) 1:500, mouse anti Tra-1-60 (Cell Signaling CS 4746) 1:500, mouse anti Tra-1-81 (Cell Signaling CS 4745) 1:500, rabbit anti-Pax6 (Covance, PRB-278P) 1:500, or mouse anti-Nestin (Abcam, ab6142) 1:1000 overnight at 4°C. Cells were washed 3 times with PBS, then incubated with AlexaFluor 488, AlexaFluor 555, and/or AlexaFluor 647 (Fisher) at 1:500 dilutions for 1 hr at RT. To stain nuclei, cells were incubated with 1:10000 Hoechst 33342 (Life Technologies). Cells were preserved in Prolong Gold anti-fade reagent (Life Technologies) and imaged on a fluorescence microscope (Z1 Axio Observer Apotome, Zeiss). Mitochondrial length was quantified using an ImageJ mitochondrial morphometry plugin as described previously (Dickey and Strack, 2011).

Stem cell modeling iPSC characterization: Standard G-banding chromosome analysis of iPSC clones was performed by Molecular Diagnostic Services (San Diego, CA). Digital karyotyping was performed by hybridization to the Illumina Infinium HumanCoreExomeBeadChip (module version 1.9.4) following the manufacturer's instructions. Analysis was performed using the cnvPartition program (Illumina) and gada R package < http://www.creal.cat/jrgonzalez/software.htm#ancla-MAD>, in addition to manual analysis.

Guide RNA design and efficacy: The target sequence for the guide RNA was designed and selected using the E-CRISP design site based on proximity to CAG repeat region and limited off-target effects (http://www.e-crisp.org/E-CRISP/). The target sequence (CGGGCCGCGGATGACGTCAGG) was incorporated into a synthesized GeneArt DNA String (Life Technologies), as described (Yang et al., 2014). This fragment and the pUC57 expression vector were simultaneously digested with EcoR1 and Pst1 restriction enzymes, ligated together, and transformed into DH5α bacteria. Surveyor nuclease assay was performed by PCR amplifying the region surrounding the putative cut site with the following primers: SCA73.1F 5′-GAGCGGAAAGAATGTCGGAGCG-3′ and SCA73.327R 5′-CAGGAACTTTGGAAGCCTCAACCC-3′. The PCR product was hybridized and treated with Surveyor Nuclease S and Surveyor Enhancer S according to manufacturer instructions (Transgenomic, Inc.).

CRISPR/Cas9 gene editing and screening: One clonal line of patient iPSCs was treated overnight with 5 uM ROCK inhibitor (Ri) (Tocris), then dissociated to single cells with Accutase (StemPro, ThermoFisher), and passed through a 40 μm nylon mesh (BD Biosciences) to ensure single cells prior to transfection. Using Human Stem Cell Nucleofector Kit 2 and Amaxa program B16 (Lonza), 2×10^6 cells were nucleofected with 9 mg of the CMV::Cas9-2A-EGFP vector or CMV::Cas9D10A-2A-EGFP (gifts from Kiran Musunuru; Addgene, #44719 and #44720) and 3 μg of the U6::gRNA vector. Transfected cells were plated in mTeSR supplemented with 5 μM Ri for 48 hr before FACS. GFP-expressing cells were selected using the BD influx at the UCSD Human Embryonic Stem Cell Core Facility. Isolated colonies were selected, expanded, and genomic DNA was extracted (DNeasy kit, QIAGEN) for PCR and sequencing analysis. All clones were initially screened by PCR using the PCRx enhancer system (Invitrogen, Life Technologies). Several clonal lines were further investigated by TOPOcloning (ThermoFisher) the PCR product, selecting 10 resulting bacterial clones, isolating DNA (QIAprep kit, QIAGEN), and sequencing (Eton Bioscience; San Diego, CA). One resulting clonal line was selected for further studies.

NPC differentiation: NPCs were generated from iPSCs described above with STEMdiff Neural Induction Medium (NIM) (StemCell Technologies) according to manufacturer's 'monolayer culture protocol' instructions and maintained in Neural Progenitor Medium (NPM) for 5-15 passages in 4% O_2/5% CO_2 at 37°C with medium changes every 2-3 days per manufacturer's instructions.

Lentivirus generation and treatment: EGFP-2A-puroR-2A, EGFP-2A-puroR-2A-Atxn7cDNA (10 CAG), and EGFP-2A-puroR-2A-Atxn7cDNA (113 CAG) cassettes were cloned into pSico lentiviral constructs. Lentiviral particles were produced using standard techniques, NPCs were transduced with lentivirus, and experiments were all performed after 48 to 72 hr.

Extracellular flux analysis: For Seahorse analysis (XF96, Agilent Technologies), NPCs were seeded at a density of 3×10^4/well in XF96 plates. After 48 hr, cells were tested for

both OCR and ECAR (extracellular acidification rate) following manufacturer's instructions with the injection of Seahorse XF Cell Mito Stress Test Kit (Agilent Technologies).

NAD^+ measurement: HeLa cells were plated at a concentration of 1.6×10^4 cells/well in a 96 well plate. Each well was transfected with lipofectamine and 0.2 ug plasmid for either cytoplasmic, nuclear, or mitochondrial NAD sensor (or cpV control) (Cambronne et al., 2016), treated with 10 nM FK866 for 11 – 18 hr, and analysis run 48-72 hr post-transfection. Each NPC line was plated at $1\text{-}2 \times 10^5$ cells/well in a 96 well plate. Each well was treated with 0.1 uL lentivirus prepared with either cytoplasmic, nuclear, or mitochondrial NAD sensor, or cpV control lentiviral vectors and analysis run 72 hr post-transduction. NPC experiments were performed 3 times as technical replicates, with 2 clones each from 2 controls or 2 SCA7 patients.

Flow cytometry analysis: Cells were prepared for analysis by removing media and dissociating with 25 uL of accutase per well (incubated at 37°C for ~10 min), followed by dilution and trituration with 100 uL of FACS buffer (PBS with 2% FBS, 2 mM EDTA, 25 mM HEPES) to single cells (125 uL total volume in each well). Analysis was performed on a BD Canto-flow cytometer with the following parameters: FSC voltage − 220, SSC voltage − 300, FITC voltage − 320, AmCyan voltage − 300. Events were recorded for 90 uL total per well. Events were gated for live cells by FSC-A x SSC-A, single cells by FSC-W x FSC-A, and then for cells that expressed the sensor by 405 nm excitation (AmCyan) x 488 nm excitation (FITC). The final gate was determined based upon a non-transfected control. Post-capture final analysis was performed using FlowJo based on the gates above. Statistics were determined using the "Derive Parameters" function for the AmCyan/FITC gate, which gave the per-cell 488/405 fluorescence ratio. The median for each well was calculated and then averaged with other wells from the same treatment/cell line.

QUANTIFICATION AND STATISTICAL ANALYSIS

All sample sizes, details, and statistical tests can be found in accompanying figure legends. Statistical analysis was done using Microsoft Excel, Prism 6.0 (GraphPad), SigmaPlot (Systat Software), Origin (Origin Labs), and galaxy workflow4metabolomics (Giacomoni et al., 2015). Statistical significance was defined at $p < 0.05$. For one-way and two-way analysis of variance (ANOVA), if statistical significance ($p < 0.05$) was achieved, then we performed post hoc analysis corresponding to the experiment, as specified, to account for multiple comparisons. All t tests were two-tailed Student's t tests, and level of significance (alpha) was always set to 0.05. Statistical analysis of metabolomics data relied upon non-parametric Wilcoxon tests, with the level of significance (alpha) also set to 0.05.

Supplementary Material

Refer to Web version on PubMed Central for supplementary material.

ACKNOWLEDGMENTS

We are grateful for the assistance and technical support provided by E. Lopez and F. Tao, to H. Zoghbi for providing SCA7 266Q knockin mice, and to X. Cambronne for providing the NAD^+ biosensors. This work was supported by funding from the NIH (R01 EY014061, R01 EY024747, and R01 AG033082 to A R.L.; R01

MH108528, R01 MH094753, R01 MH109885, R01 MH100175, U19 MH107367, and a NARSAD Independent Investigator Grant to A.R.M.; and R01 NS084217 to R.S.M.) and the California Institute for Regenerative Medicine (DISC1-08825 to A.R.M. and CIRM TG2-01154 to J.M.W.). The SCA7 patient study was supported by funding from the French Ministry of Health (PHRC BIOSCA - ID RCB: 2010-A01324-35), the program “Investissements d’avenir” ANR-10-IAIHU-06, and the patients’ association Connaître les Syndromes Cérébelleux (CSC). This work was also supported by the Waitt Advanced Biophotonics Core Facility of the Salk Institute with funding from the NIH-NCI CCSG (P30 014195); NINDS Neuroscience Core Grant NS072031; and the Waitt Foundation, with assistance from C. Peto and S. Dunn. R.M.E. is an Investigator of the Howard Hughes Medical Institute at the Salk Institute and March of Dimes Chair in Molecular and Developmental Biology. P.M.S. was supported by a mobility grant from the Polish Ministry of Science and Higher Education (1303/MOB/IV/2015/0: Mobilnosc Plus).

REFERENCES

Adanyeguh IM, Rinaldi D, Henry PG, Caillet S, Valabregue R, Durr A, and Mochel F (2015). Triheptanoin improves brain energy metabolism in patients with Huntington disease. Neurology 84, 490–495. [PubMed: 25568297]

Ansorge O, Giunti P, Michalik A, Van Broeckhoven C, Harding B, Wood N, and Scaravilli F (2004). Ataxin-7 aggregation and ubiquitination in infantile SCA7 with 180 CAG repeats. Ann. Neurol. 56, 448–52. [PubMed: 15349877]

Cambronne XA, Stewart ML, Kim D, Jones-Brunette AM, Morgan RK, Farrens DL, Cohen MS, and Goodman RH (2016). Biosensor reveals multiple sources for mitochondrial NAD^+. Science 352, 1474–1477. [PubMed: 27313049]

Chailangkarn T, Trujillo CA, Freitas BC, Hrvoj-Mihic B, Herai RH, Yu DX, Brown TT, Marchetto MC, Bardy C, McHenry L, et al. (2016). A human neurodevelopmental model for Williams syndrome. Nature 536,338–343. [PubMed: 27509850]

Chance B, Eleff S, Leigh JS, Jr., Sokolow D, and Sapega A (1981). Mitochondrial regulation of phosphocreatine/inorganic phosphate ratios in exercising human muscle: a gated 31P NMR study. Proc. Natl. Acad. Sci. U S A 78, 6714–6718. [PubMed: 6947247]

Cooles P, Michaud R, and Best PV (1988).Adominantly inherited progressive disease in a black family characterised by cerebellar and retinal degeneration, external ophthalmoplegia and abnormal mitochondria. J. Neurol. Sci. 87, 275–288. [PubMed: 3210038]

David G, Abbas N, Stevanin G, Dürr A, Yvert G, Cancel G, Weber C, Imbert G, Saudou F, Antoniou E, et al. (1997). Cloning of the SCA7 gene reveals a highly unstable CAG repeat expansion. Nat. Genet. 17, 65–70. [PubMed: 9288099]

Dickey AS, and Strack S (2011). PKA/AKAP1 and PP2A/Bβ2 regulate neuronal morphogenesis via Drp1 phosphorylation and mitochondrial bioener-getics. J. Neurosci. 31, 15716–15726. [PubMed: 22049414]

DiMauro S, and Schon EA (2003). Mitochondrial respiratory-chain diseases. N. Engl. J. Med. 348, 2656–2668. [PubMed: 12826641]

Filosto M, Scarpelli M, Cotelli MS, Vielmi V, Todeschini A, Gregorelli V, Tonin P, Tomelleri G, and Padovani A (2011). The role of mitochondria in neurodegenerative diseases. J. Neurol. 258, 1763–1774. [PubMed: 21604203]

Forsgren L, Libelius R, Holmberg M, von Döbeln U, Wibom R, Heijbel J, Sandgren O, and Holmgren G (1996). Muscle morphology and mitochondrial investigations of a family with autosomal dominant cerebellar ataxia and retinal degeneration mapped to chromosome 3p12-p21.1. J. Neurol. Sci. 144,91–98. [PubMed: 8994109]

Garali I, Adanyeguh IM, Ichou F, Perlbarg V, Seyer A, Colsch B, Moszer I, Guillemot V, Durr A, Mochel F, et al. (2017). A strategy for multimodal data integration: application to biomarkers identification in spinocerebellar ataxia. Brief. Bioinform. 19, 1356–1369.

Garden G (1993).Spinocerebellar Ataxia Type7 In GeneReviews(R), Pagon RA, Adam MP, Ardinger HH, Wallace SE, Amemiya A, Bean LJH, Bird TD, Fong CT, Mefford HC, and Smith RJH, et al., eds. (Seattle: WA).

Garden GA, and La Spada AR (2008). Molecular pathogenesis and cellular pathology of spinocerebellar ataxia type 7 neurodegeneration. Cerebellum 7, 138–149. [PubMed: 18418675]

Gatchel JR, Watase K, Thaller C, Carson JP, Jafar-Nejad P, Shaw C, Zu T, Orr HT, and Zoghbi HY (2008). The insulin-like growth factor pathway is altered in spinocerebellar ataxia type 1 and type 7. Proc. Natl. Acad. Sci. U S A 105, 1291–1296. [PubMed: 18216249]

Giacomoni F, Le Corguillé G, Monsoor M, Landi M, Pericard P, Pétéra M, Duperier C, Tremblay-Franco M, Martin JF, Jacob D, et al. (2015). Workflow4Metabolomics: a collaborative research infrastructure for computational metabolomics. Bioinformatics 31, 1493–1495. [PubMed: 25527831]

Girard M, Larivière R, Parfitt DA, Deane EC, Gaudet R, Nossova N, Blondeau F, Prenosil G, Vermeulen EG, Duchen MR, et al. (2012). Mitochondrial dysfunction and Purkinje cell loss in autosomal recessive spastic ataxia of Charlevoix-Saguenay (ARSACS). Proc. Natl. Acad. Sci. U S A 109, 1661–1666. [PubMed: 22307627]

Golpich M, Amini E, Mohamed Z, Azman Ali R, Mohamed Ibrahim N, and Ahmadiani A (2017). Mitochondrial dysfunction and biogenesis in neurodegenerative diseases: pathogenesis and treatment. CNS Neurosci. Ther. 23, 5–22. [PubMed: 27873462]

Guarente L (2016). Cell metabolism. The resurgence of NAD^+. Science 352, 1396–1397. [PubMed: 27313027]

Guyenet SJ, Furrer SA, Damian VM, Baughan TD, La Spada AR, and Garden GA (2010). A simple composite phenotype scoring system for evaluating mouse models of cerebellar ataxia. J. Vis. Exp Published online 5 21, 2010. 10.3791/1787

Hamilton J, Pellman JJ, Brustovetsky T, Harris RA, and Brustovetsky N (2015). Oxidative metabolism in YAC128 mouse model of Huntington's disease. Hum. Mol. Genet. 24, 4862–4878. [PubMed: 26041817]

Han Y, Deng B, Liu M, Jiang J, Wu S, and Guan Y (2010). Clinical and genetic study of a Chinese family with spinocerebellar ataxia type 7. Neurol. India 58, 622–626. [PubMed: 20739808]

Heigwer F, Kerr G, and Boutros M (2014). E-CRISP:fast CRISPR target site identification. Nat. Methods 11, 122–123. [PubMed: 24481216]

Helmlinger D, Hardy S, Sasorith S, Klein F, Robert F, Weber C, Miguet L, Potier N, Van-Dorsselaer A, Wurtz JM, et al. (2004). Ataxin-7 is a subunit of GCN5 histone acetyltransferase-containing complexes. Hum. Mol. Genet. 13, 1257–1265. [PubMed: 15115762]

Howarth C, Peppiatt-Wildman CM, and Attwell D (2010). The energy use associated with neural computation in the cerebellum. J. Cereb. Blood Flow Metab. 30, 403–14. [PubMed: 19888288]

Kelly DP, and Scarpulla RC (2004). Transcriptional regulatory circuits controlling mitochondrial biogenesis and function. Genes Dev. 18, 357–368. [PubMed: 15004004]

Knott AB, Perkins G, Schwarzenbacher R, and Bossy-Wetzel E (2008). Mitochondrial fragmentation in neurodegeneration. Nat. Rev. Neurosci. 9, 505–518. [PubMed: 18568013]

La Spada AR, Fu YH, Sopher BL, Libby RT, Wang X, Li LY, Einum DD, Huang J, Possin DE, Smith AC, et al. (2001). Polyglutamine-expanded ataxin-7 antagonizes CRX function and induces cone-rod dystrophy in a mouse model of SCA7. Neuron 31, 913–927. [PubMed: 11580893]

Lim S, Honek J, Xue Y, Seki T, Cao Z, Andersson P, Yang X, Hosaka K, and Cao Y (2012). Cold-induced activation of brown adipose tissue and adipose angiogenesis in mice. Nat. Protoc. 7, 606–615. [PubMed: 22383039]

Lin MT, and Beal MF (2006). Mitochondrial dysfunction and oxidative stress in neurodegenerative diseases. Nature 443, 787–795. [PubMed: 17051205]

Long AN, Owens K, Schlappal AE, Kristian T, Fishman PS, and Schuh RA (2015). Effect of nicotinamide mononucleotide on brain mitochondrial respiratory deficits in an Alzheimer's disease-relevant murine model. BMC Neurol. 15, 19. [PubMed: 25884176]

Martin JJ, Van Regemorter N, Krols L, Brucher JM, de Barsy T, Szliwowski H, Evrard P, Ceuterick C, Tassignon MJ, Smet-Dieleman H, et al. (1994). On an autosomal dominant form of retinal-cerebellar degeneration: an autopsy study of five patients in one family. Acta Neuropathol. 88, 277–286. [PubMed: 7839819]

Michalik A, Martin JJ, and Van Broeckhoven C (2004). Spinocerebellar ataxia type 7 associated with pigmentary retinal dystrophy. Eur. J. Hum. Genet. 12, 2–15. [PubMed: 14571264]

Mishra P, and Chan DC (2016). Metabolic regulation of mitochondrial dynamics. J. Cell Biol. 212, 379–387. [PubMed: 26858267]

Mochel F, N'Guyen TM, Deelchand D, Rinaldi D, Valabregue R, Wary C, Carlier PG, Durr A, and Henry PG (2012). Abnormal response to cortical activation in early stages of Huntington disease. Mov. Disord. 27, 907–910. [PubMed: 22517114]

Modi G (2000). Morphological abnormalities of hepatic mitochondria in two patients with spinocerebellar ataxia type 7. J. Neurol. Neurosurg. Psychiatry 68, 393–394. [PubMed: 10787310]

Narendra DP, and Youle RJ (2012). Neurodegeneration:trouble in the cell's powerhouse. Nature 483, 418–419. [PubMed: 22398449]

Palhan VB, Chen S, Peng GH, Tjernberg A, Gamper AM, Fan Y, Chait BT, La Spada AR, and Roeder RG (2005). Polyglutamine-expanded ataxin-7 inhibits STAGA histone acetyltransferase activity to produce retinal degeneration. Proc. Natl. Acad. Sci. U S A 102, 8472–8477. [PubMed: 15932940]

Paulson HL, Bonini NM, and Roth KA (2000). Polyglutamine disease and neuronal cell death. Proc. Natl. Acad. Sci. U S A 97, 12957–12958. [PubMed: 11058149]

Rafelski SM (2013). Mitochondrial network morphology: building an integrative, geometrical view. BMC Biol. 11, 71. [PubMed: 23800141]

Ramachandran PS, Boudreau RL, Schaefer KA, La Spada AR, and Davidson BL (2014). Nonallele specific silencing of ataxin-7 improves disease phenotypes in a mouse model of SCA7. Mol. Ther. 22, 1635–1642. [PubMed: 24930601]

Ramachandran S, Haddad D, Li C, Le MX, Ling AK, So CC, Nepal RM, Gommerman JL, Yu K, Ketela T, et al. (2016). The SAGA deubiquitination module promotes DNA repair and class switch recombination through ATM and DNAPK-mediated γH2AX formation. Cell Rep. 15, 1554–1565. [PubMed: 27160905]

Revollo JR, Grimm AA, and Imai S (2004). The NAD biosynthesis pathway mediated by nicotinamide phosphoribosyltransferase regulates Sir2 activity in mammalian cells. J. Biol. Chem. 279, 50754–50763. [PubMed: 15381699]

Rodgers JT, Lerin C, Haas W, Gygi SP, Spiegelman BM, and Puig-server P (2005). Nutrient control of glucose homeostasis through a complex of PGC-1alpha and SIRT1. Nature 434, 113–118. [PubMed: 15744310]

Ross CA (1997). Intranuclear neuronal inclusions: a common pathogenic mechanism for glutamine-repeat neurodegenerative diseases? Neuron 19, 1147–1150. [PubMed: 9427237]

Rustin P, Parfait B, Chretien D, Bourgeron T, Djouadi F, Bastin J, Rötig A, and Munnich A (1996). Fluxes of nicotinamide adenine dinucleotides through mitochondrial membranes in human cultured cells. J. Biol. Chem. 271, 14785–14790. [PubMed: 8663005]

Ryu D, Zhang H, Ropelle ER, Sorrentino V, Mázala DA, Mouchiroud L, Marshall PL, Campbell MD, Ali AS, Knowels GM, et al. (2016). NAD+ repletion improves muscle function in muscular dystrophy and counters global PARylation. Sci. Transl. Med 8, 361ra139.

Scheibye-Knudsen M, Scheibye-Alsing K, Canugovi C, Croteau DL, and Bohr VA (2013). A novel diagnostic tool reveals mitochondrial pathology in human diseases and aging. Aging (Albany N.Y.) 5, 192–208.

Scoles DR, Meera P, Schneider MD, Paul S, Dansithong W, Figueroa KP, Hung G, Rigo F, Bennett CF, Otis TS, and Pulst SM (2017). Antisense oligonucleotide therapy for spinocerebellar ataxia type 2. Nature 544, 362–366. [PubMed: 28405024]

Sesaki H, and Jensen RE (1999). Division versus fusion: Dnm1p and Fzo1p antagonistically regulate mitochondrial shape. J. Cell Biol. 147, 699–706. [PubMed: 10562274]

Stevanin G, Dürr A, and Brice A (2000). Clinical and molecular advances in autosomal dominant cerebellar ataxias: from genotype to phenotype and physiopathology. Eur. J. Hum. Genet. 8, 4–18. [PubMed: 10713882]

Takahashi K, and Yamanaka S (2006). Induction of pluripotent stem cells from mouse embryonic and adult fibroblast cultures by defined factors. Cell 126, 663–676. [PubMed: 16904174]

Takahashi K, Tanabe K, Ohnuki M, Narita M, Ichisaka T, Tomoda K, and Yamanaka S (2007). Induction of pluripotent stem cells from adult human fibroblasts by defined factors. Cell 131, 861–872. [PubMed: 18035408]

Thomas CA, Tejwani L, Trujillo CA, Negraes PD, Herai RH, Mesci P, Macia A, Crow YJ, and Muotri AR (2017). Modeling of TREX1-dependent autoimmune disease using human stem cells

highlights L1 accumulation as a source of neuroinflammation. Cell Stem Cell 21, 319–331.e8. [PubMed: 28803918]

To KW, Adamian M, Jakobiec FA, and Berson EL (1993). Olivopontocerebellar atrophy with retinal degeneration. An electroretinographic and histopathologic investigation. Ophthalmology 100, 15–23. [PubMed: 8433819]

van de Warrenburg BP, Frenken CW, Ausems MG, Kleefstra T, Sinke RJ, Knoers NV, and Kremer HP (2001). Striking anticipation in spinocerebellar ataxia type 7: the infantile phenotype. J. Neurol. 248, 911–914. [PubMed: 11697534]

Wang X, Hu X, Yang Y, Takata T, and Sakurai T (2016). Nicotinamide mononucleotide protects against β-amyloid oligomer-induced cognitive impairment and neuronal death. Brain Res. 1643, 1–9. [PubMed: 27130898]

Westermann B (2012). Bioenergetic role of mitochondrial fusion and fission. Biochim. Biophys. Acta 1817, 1833–1838. [PubMed: 22409868]

Weydt P, Pineda VV, Torrence AE, Libby RT, Satterfield TF, Lazarowski ER, Gilbert ML, Morton GJ, Bammler TK, Strand AD, et al. (2006). Thermoregulatory and metabolic defects in Huntington's disease transgenic mice implicate PGC-1alpha in Huntington's disease neurodegeneration. Cell Metab. 4, 349–362. [PubMed: 17055784]

Whitney A, Lim M, Kanabar D, and Lin JP (2007). Massive SCA7 expansion detected in a 7-month-old male with hypotonia, cardiomegaly, and renal compromise. Dev. Med. Child Neurol. 49, 140–143. [PubMed: 17254003]

Wiener DH, Fink LI, Maris J, Jones RA, Chance B, and Wilson JR (1986). Abnormal skeletal muscle bioenergetics during exercise in patients with heart failure: role of reduced muscle blood flow. Circulation 73, 1127–1136. [PubMed: 3698247]

Williams PA, Harder JM, Foxworth NE, Cochran KE, Philip VM, Porciatti V, Smithies O, and John SW (2017). Vitamin B3 modulates mitochondrial vulnerability and prevents glaucoma in aged mice. Science 355,756–760. [PubMed: 28209901]

Yang L, Mali P, Kim-Kiselak C, and Church G (2014). CRISPR-Cas-mediated targeted genome editing in human cells. Methods Mol. Biol. 1114, 245–267. [PubMed: 24557908]

Yoo SY, Pennesi ME, Weeber EJ, Xu B, Atkinson R, Chen S, Armstrong DL, Wu SM, Sweatt JD, and Zoghbi HY (2003). SCA7 knockin mice model human SCA7 and reveal gradual accumulation of mutant ataxin-7 in neurons and abnormalities in short-term plasticity. Neuron 37, 383–401. [PubMed: 12575948]

Highlights

- SCA7 patients display impaired oxidative metabolism on magnetic resonance spectroscopy
- Oxygen consumption and respiration are markedly decreased in SCA7 model mice
- Mitochondrial fragmentation occurs in SCA7 mouse Purkinje cells and iPSC-derived neurons
- NAD^+ is markedly reduced in nucleus and mitochondria of SCA7 patient-derived neurons

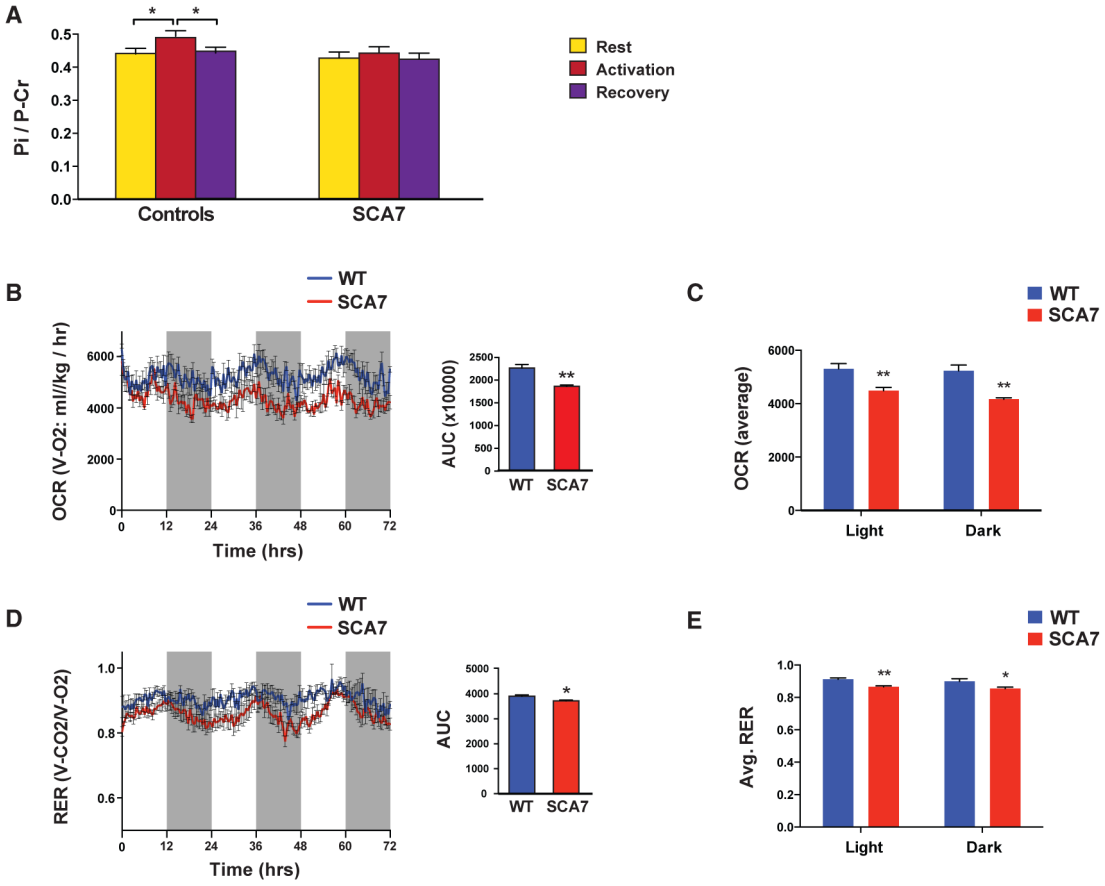

Figure 1. Both SCA7 Patients and SCA7 Mice Exhibit Impaired Metabolic Respiration

(A) Results of ^{31}P functional magnetic resonance spectroscopy on 12 spinocerebellar ataxia 7 (SCA7) patients and 13 normal controls during performance of a visual task. A significant increase in the ratio of inorganic phosphate to phosphocreatinine (Pi/P-Cr) during performance of the visual task in comparison with recovery occurred for normal controls, but no change in Pi/P-Cr was noted for SCA7 patients. *$p < 0.05$ (two-tailed t test). Error bars represent within-subject differences of corrected SEM on normalized data.

(B) Metabolic cage measurement of the oxygen consumption rate (VO_2; mL/kg/h) quantified by area under the curve (AUC) over the course of 72 h. White panels indicate light (day) periods, and gray panels indicate dark (night) periods; 8.5-week-old wild-type (WT) control and SCA7 mice; n = 5 mice/genotype; **$p < 0.01$ (two-tailed t test). Error bars indicate SEM.

(C) Quantification of average measurements of oxygen consumption rate (OCR) during light and dark intervals from (B). **$p < 0.01$ (two-tailed t test). Error bars indicate SEM.

(D) Respiratory exchange ratio (RER) (CO_2 emission/O_2 consumption), quantified by area under the curve (AUC) over the course of 72 h. White panels indicate light (day) periods, and gray panels indicate dark (night) periods; 8.5-week-old WT and SCA7 mice; n = 5 mice/genotype; *$p < 0.05$ (two-tailed t test). Error bars indicate SEM.

(E) Quantification of average measurements of RER during light and dark intervals from (D). *$p < 0.05$ and **$p < 0.01$ (two-tailed t test). Error bars indicate SEM.

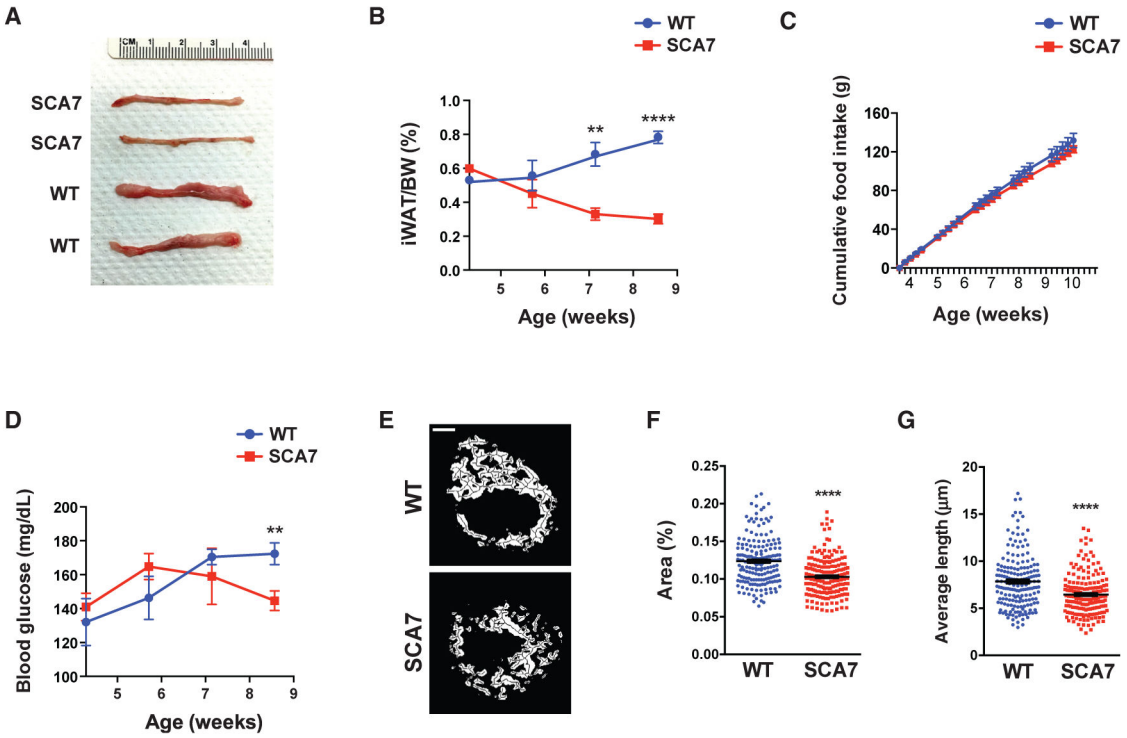

Figure 2. SCA7 Mice Exhibit Reduced Fat Stores, Decreased Blood Glucose Levels, and Altered Mitochondrial Network Integrity

(A) Representative images of inguinal white adipose tissue (iWAT) from two SCA7 and two WT mice at 8.5 weeks of age.

(B) iWAT was dissected and weighed as a proportion of body weight at indicated ages. WT and SCA7 mice; n = 3–6 mice/genotype at 30, 40, and 50 days of age; n = 20 mice/genotype at 60 days of age; **p < 0.01 and ****p < 0.0001 (two-tailed t test).

(C) Cumulative food intake over time course for WT and SCA7 mice; n = 3 mice/genotype.

(D) Blood glucose levels after 6 h of fasting at indicated ages. WT and SCA7 mice; n = 3–6 mice/genotype at 30, 40, and 50 days of age; n = 20 mice/genotype at 60 days of age; **p < 0.01 (two-tailed t test).

(E) Representative images of skeletonized Tom20 signal within a Purkinje cell body to exhibit extremes of length measurement. The average length of the depicted WT mitochondria is 14 µm, while average length of the depicted SCA7 mitochondria is 5 µm. Scale bar, 5 µm

(F) Quantification of average mitochondrial content by measuring Tom20 immunofluorescence signal as a percentage of calbindin immunofluorescence. Data are represented as mean ± SEM, and each dot represents the result for an individual Purkinje cell soma; 8.5-week-old WT and SCA7 mice; n = 3 mice/genotype, n = 180–190 cells/genotype; ****p < 0.0001 (two-tailed t test).

(G) Quantification of average length of the mitochondrial network. Data are represented as mean ± SEM, and each dot represents the results for an individual Purkinje cell soma; 8.5-week-old WT and SCA7 mice; n = 3 mice/genotype, n = 180–190 cells/genotype; ****p < 0.0001 (two-tailed t test). Error bars indicate SEM.

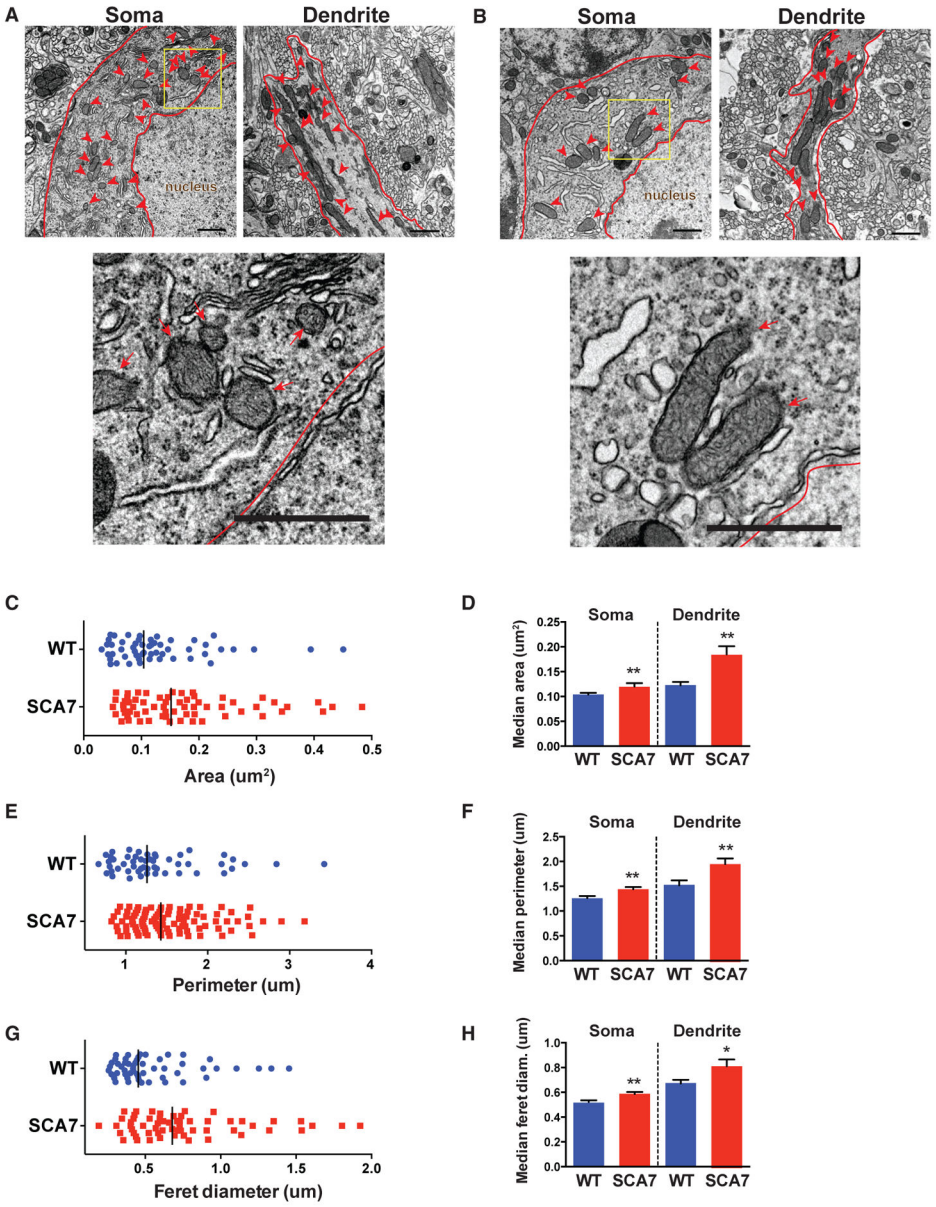

Figure 3. SCA7 Purkinje Cells Display Abnormal Mitochondrial Morphology

(A) Representative images of WT Purkinje cell soma and dendrites at 8.5 weeks of age. Red arrowheads indicate mitochondria. Red outlines demarcate the cytosol of a Purkinje cell soma and dendrite to delineate the analyzed area. Bottom: zoom of the yellow boxed region. Scale bars, 1 μm.

(B) Representative images of SCA7 Purkinje cell soma and dendrites at 8.5 weeks of age. Red arrowheads indicate mitochondria. Red outlines demarcate the cytosol of a Purkinje cell soma and dendrite to delineate the analyzed area. Bottom: zoom of the yellow boxed region. Scale bars, 1 μm.

(C) Representative graph of the area of individual mitochondria within a single Purkinje cell soma from (A) and (B). Each dot represents an individual mitochondrion;black bars represent the medians.

(D) Quantification of the medians represented in (C) from the soma and dendrites of analyzed Purkinje cells; 8.5-week-old WT and SCA7 mice; n = 3 mice/genotype, n = 12–19 cells/genotype; **$p < 0.01$ and ***$p < 0.001$ (two-tailed t test).

(E) Representative graph of the perimeter of individual mitochondria within a single Purkinje cell soma from (A) and (B). Each dot represents an individual mitochondrion; black bars represent the medians.

(F) Quantification of the medians represented in (E) from the soma and dendrites of analyzed Purkinje cells; 8.5-week-old WT and SCA7 mice; n = 3 mice/genotype, n = 12–19 cells/genotype; *$p < 0.05$ and ***$p < 0.001$ (two-tailed t test).

(G) Representative graph of the feret diameter of individual mitochondria within a single Purkinje cell soma from (A) and (B). Each dot represents an individual mitochondrion; black bars represent the medians.

(H) Quantification of the medians represented in (G) from the soma and dendrites of analyzed Purkinje cells; 8.5-week-old WT and SCA7 mice; n = 3 mice/genotype, n = 12–19 cells/genotype; *$p < 0.05$ and ***$p < 0.001$ (two-tailed t test). Error bars indicate SEM.

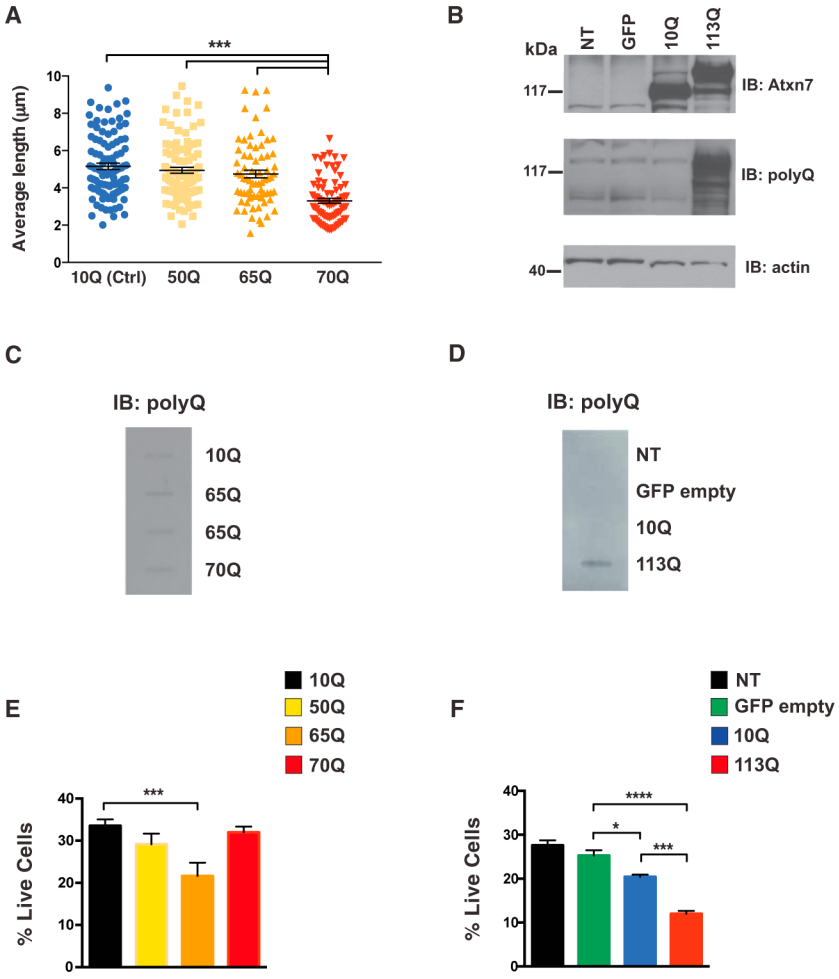

Figure 4. SCA7 Stem Cell Neural Derivatives Exhibit PolyQ Length-Dependent Disease Phenotypes

(A) Graph of average mitochondrial length of control (10Q) and SCA7 patient (50Q, 65Q, 70Q) neuronal progenitor cells (NPCs) on the basis of Tom20 immunostaining. Quantification of average mitochondrial length analyzed using ImageJ mitochondrial morphometry plugin. Each dot represents the average mitochondrial length from an individual cell, and data are represented as mean ± SEM. Two control patient lines (one or two clones per line) and two SCA7 patient lines (two clones per line); n = 70–100 cells/genotype. ***$p < 0.001$ (one-way ANOVA with post hoc Tukey's multiple-comparison test).

(B) Ataxin-7-knockout NPCs were transduced with empty vector, ataxin-7-10Q, or ataxin-7-113Q lentivirus vector. Non-transduced (NT) cells serve as a negative control for transfection. Protein lysates were immunoblotted with anti-ataxin-7 or antiexpanded polyQ tract antibody, as indicated. β-Actin immunoblotting analysis was performed as a loading control.

(C) Protein lysates from control and SCA7 patient NPCs of the indicated CAG repeat allele size were filtered through nitrocellulose and then immuno-blotted with anti-expanded polyQ tract antibody.

(D) Protein lysates from non-transduced ataxin-7-knockout NPCs or from ataxin-7-knockout NPCs transduced with empty vector, ataxin-7-10Q, or ataxin-7-113Q lentivirus vector were filtered through nitrocellulose and then immunoblotted with anti-expanded polyQ tract antibody.

(E) Control and SCA7 patient NPCs of the indicated CAG repeat allele size were analyzed for percentage of live cells by fluorescence-activated cell sorting (FACS) for side scatter (SSC-A) and forward scatter (FSC-A). n = 2 clones/genotype except for SCA7 50Q, for which one clone was available; n = 8 replicates/clone. ***$p < 0.001$ (one-way ANOVA with post hoc Tukey's multiple-comparison test).

(F) Non-transduced ataxin-7-knockout NPCs or ataxin-7-knockout NPCs transduced with empty vector, ataxin-7-10Q, or ataxin-7-113Q lentivirus vector were analyzed for percentage of live cells by FACS for side scatter (SSC-A) and forward scatter (FSC-A). Isogenic lines, one clone per genotype, n = 3 technical replicates. *$p < 0.05$, ***$p < 0.001$, and ****$p < 0.0001$ (ordinary one-way ANOVA with post hoc Tukey's multiple-comparison test). Error bars indicate SEM.

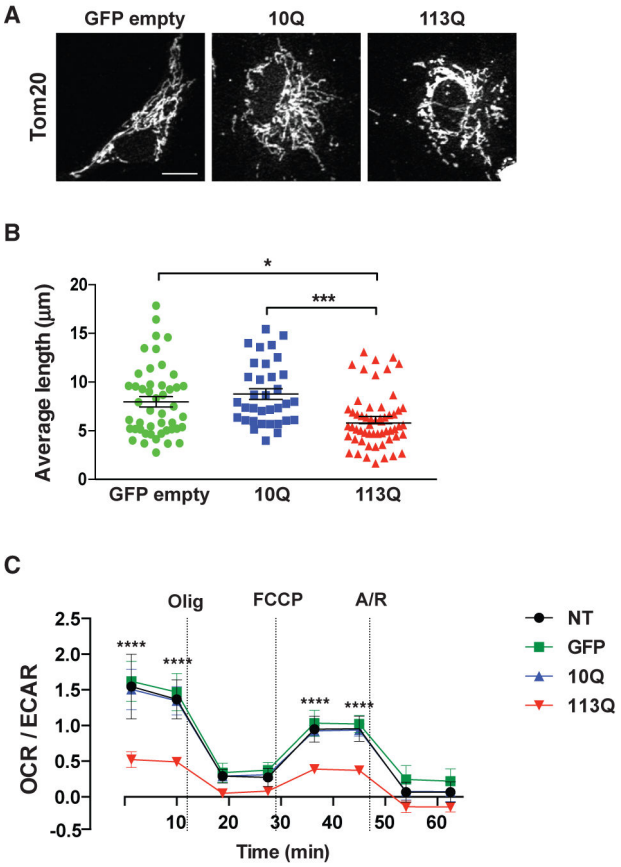

Figure 5. SCA7 Stem Cell Neural Derivatives Display PolyQ Length-Dependent Mitochondrial Morphology and Metabolic Defects

(A) Representative images of Tom20 immunostaining for ataxin-7-knockout NPCs transduced with empty vector, ataxin-7-10Q, or ataxin-7-113Q lentivirus vector. Scale bar, 5 μm.

(B) Quantification of average mitochondrial length on the basis of Tom20 immunostaining and ImageJ mitochondrial morphometry analysis. Each dot represents an individual cell, data are represented as mean ± SEM. Isogenic lines, one clone per genotype, n = 34–57 cells/genotype. *$p < 0.05$ and ***$p < 0.001$ (one-way ANOVA with post hoc Tukey's multiple-comparison test).

(C) Extracellular flux analysis to measure oxygen consumption rate (OCR) as a function of extracellular acidification rate (ECAR) for non-transduced ataxin-7-knockout NPCs or ataxin-7-knockout NPCs transduced with empty vector, ataxin-7-10Q, or ataxin-7-113Q lentivirus vector.

Oligomycin, FCCP, or antimycin/rotenone (A/R) treatments were given at the indicated time points. Data are represented as mean ± SEM. Isogenic lines, one clone per genotype, n = 5 wells/genotype. Two-way ANOVA with post hoc Dunnett's multiple-comparison test at each time point. Asterisks indicate comparison between ataxin-7-113Q and each other genotype condition (****$p < 0.0001$). Error bars indicate SEM.

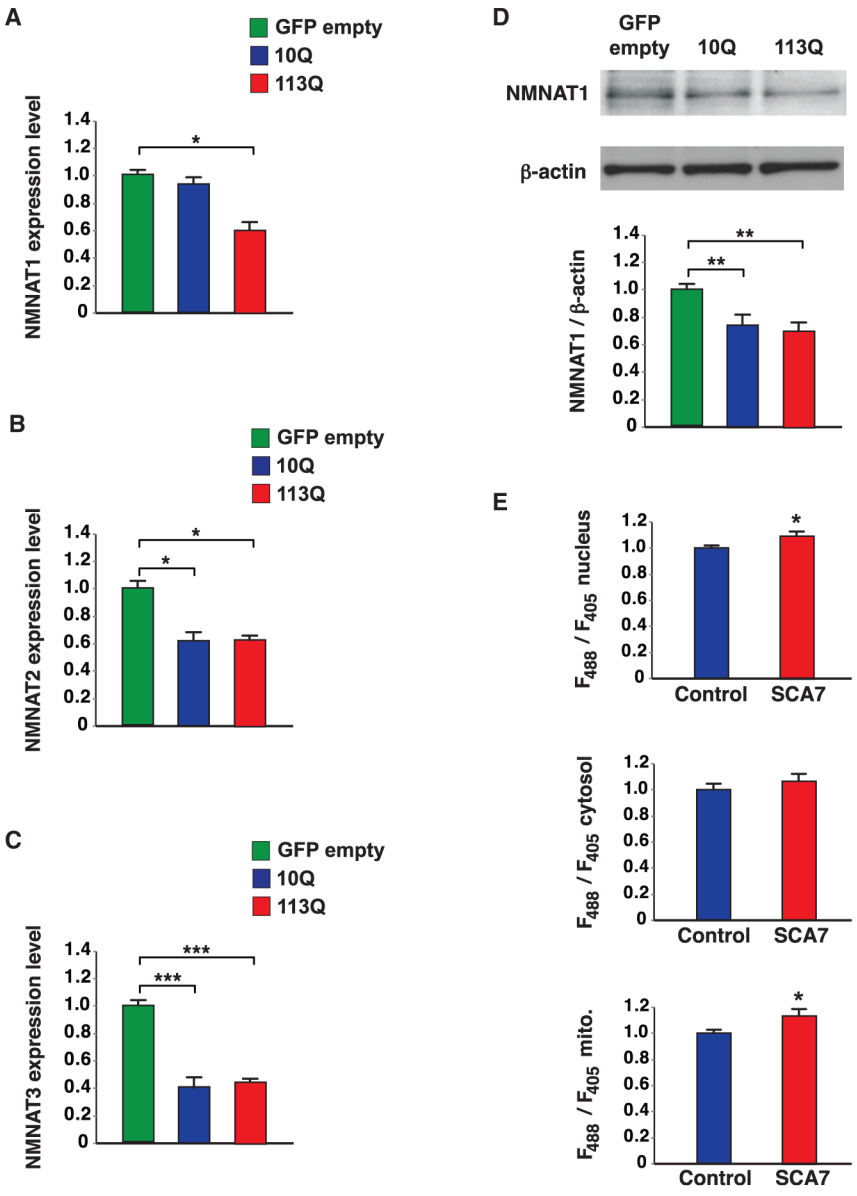

Figure 6. SCA7 Stem Cell Neural Derivatives Exhibit Altered NAD$^+$ Salvage Pathway Enzyme Expression and Reduced NAD$^+$ Levels in the Nucleus and Mitochondria

(A) qRT-PCR analysis of NMNAT1 gene expression for ataxin-7-knockout NPCs transduced with empty vector, ataxin-7-10Q, or ataxin-7-113Q lentivirus vector. Isogenic lines, one clone per genotype, n = 3/genotype. *p < 0.05 (one-way ANOVA with post hoc Tukey's multiple-comparison test).

(B) qRT-PCR analysis of NMNAT2 gene expression for ataxin-7-knockout NPCs transduced with empty vector, ataxin-7-10Q, or ataxin-7-113Q lentivirus vector. One clone per genotype (all on isogenic background), n = 3/genotype. *p < 0.05 (one-way ANOVA with post hoc Tukey's multiple-comparison test).

(C) qRT-PCR analysis of NMNAT3 gene expression for ataxin-7-knockout NPCs transduced with empty vector, ataxin-7-10Q, or ataxin-7-113Q lentivirus vector. One clone per genotype

(all on isogenic background), n = 3/genotype. ***p < 0.001 (one-way ANOVA with post hoc Tukey's multiple-comparison test).

(D) NMNAT1 immunoblot analysis of protein lysates from ataxin-7-knockout NPCs transduced with empty vector, ataxin-7-10Q, or ataxin-7-113Q lentivirus vector. β-Actin immunoblot served as a loading control. Bottom: quantification of NMNAT1 protein expression normalized to β-actin. **p < 0.01 (one-way ANOVA with post hoc Tukey's multiple-comparison test).

(E) SCA7 patient NPCs or control NPCs were transfected with a nicotinamide adenine dinucleotide (NAD^+) biosensor linked to a nuclear localization signal (top), cytosolic localization signal (middle), or mitochondrial localization signal (bottom). After excitation at 488 nm to monitor NAD^+ binding, which reduces fluorescence, and excitation at 405 nm, which elicits fluorescence in the absence of NAD^+ binding to normalize sensor expression level, we calculated the emission ratio for SCA7 patient NPCs and control NPCs. An increased fluorescence ratio for SCA7 patient NPCs indicated a reduced level of NAD^+. NPC lines, two clones per genotype, n = 2/genotype; n = 3 technical replicates. *p < 0.05 (unpaired t test). Error bars indicate SEM.

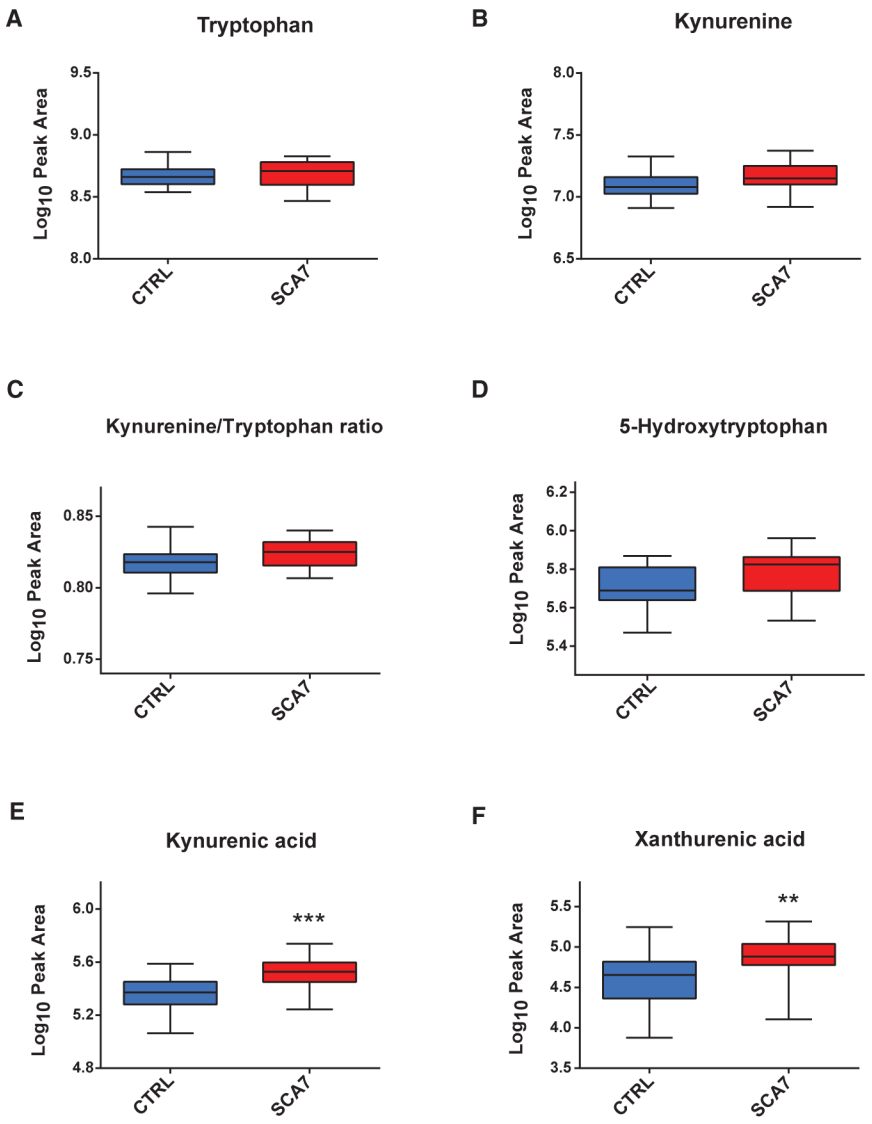

Figure 7. Metabolomics Analysis Reveals Altered Tryptophan Metabolism in SCA7 Patients

(A–F) We performed high-resolution mass spectrometry in combination with liquid chromatography (LC-HRMS) on plasma samples from 13 fasted SCA7 patients and 35 fasted controls. Depicted are boxplot representations for analyte signal areas in $\log_{10}$, corresponding to (A) tryptophan, (B) kynurenine, (C) kynurenine/tryptophan ratio, (D) 5-hydroxytryptophan, (E) kynurenic acid, and (F) xanthurenic acid. $^{**}p < 0.01$ and $^{***}p < 0.001$ (two-tailed t test). Error bars indicate SEM.

KEY RESOURCES TABLE

REAGENT or RESOURCE	SOURCE	IDENTIFIER
Antibodies		
Mouse anti-Calbindin	Sigma-Aldrich	Cat# C9848; RRID:AB_476894
Rabbit anti-Tom20	Santa Cruz	Cat# sc-11415; RRID:AB_2207533
Anti-mouse superclonal AlexaFluor 488	Fisher	Cat# A28175; RRID:AB_2536161
Anti-rabbit AlexaFluor 555	Fisher	Cat# A-21428; RRID:AB_2535849
Anti-rabbit AlexaFluor 647	Fisher	Cat# A27040; RRID:AB_2536101
Rabbit anti-ATXN7	Thermo	Cat# PA1-749; RRID:AB_2061308
Mouse anti-polyQ 1C2	Millipore	Cat# MAB1574; RRID:AB_94263
Rabbit anti-TOMM20	Novus	Cat# NBP1-81556; RRID:AB_11003249
Mouse anti-MFN1	Abcam	Cat# ab57602; RRID:AB_2142624
Mouse anti-DRP1	Abcam	Cat# ab56788; RRID:AB_941306
Mouse anti-beta actin	Abcam	Cat# ab8226; RRID:AB_306371
Anti-mouse HRP secondary antibody	Santa Cruz	Cat# sc-2005; RRID:AB_631736
Anti-rabbit HRP secondary antibody	Santa Cruz	Cat# sc-2004; RRID:AB_631746
Chicken anti-GFP	Abcam	Cat# ab13970; RRID:AB_300798
Mouse anti-SSEA4	Cell Signaling	Cat# 4755; RRID:AB_1264259
Mouse anti Tra-1-60	Cell Signaling	Cat# 4746; RRID:AB_2119059
Mouse anti Tra-1-81	Cell Signaling	Cat# 4745; RRID:AB_2119060
Rabbit anti-Pax6	Covance	Cat# PRB-278P; RRID:AB_291612
Mouse anti-Nestin	Abcam	Cat# ab6142; RRID:AB_305313
Bacterial and Virus Strains		
DH5-a	Life Technologies	18265017
Biological Samples		
Patient and control primary fibroblasts	This paper	N/A
Chemicals, Peptides, and Recombinant Proteins		
mTesR1 medium	Stem Cell Technologies	Cat. 85850
Matrigel	BD Biosciences	356234
Prolong Gold anti-fade reagent	ThermoFisher	P36930
cOmplete ULTRA mini protease inhibitor	Roche	5892791001
GE Healthcare Amersham ECL Prime Western Blotting Detection Reagent	Denville Scientific	E3018
ROCK inhibitor (Ri) Y-27632 dihydrochloride	Tocris	125410
Accutase	ThermoFisher	A1110501
STEMdiff Neural Induction Medium	StemCell Technologies	05835
STEMdiff Neural Progenitor Medium	StemCell Technologies	05833
FK866 chemical	Life Technologies	XP00165BOX
Hoechst 33342	Life Technologies	H3570

REAGENT or RESOURCE	SOURCE	IDENTIFIER
Critical Commercial Assays		
TURBO DNA-free kit	ThermoFisher	AM1907
High-Capacity cDNA Reverse Transcription Kit	ThermoFisher	4368814
TaqMan Universal Master Mix II	Life Technologies	4440040
BCA assay	Pierce; ThermoFisher	23225
Surveyor Nuclease Kit	Transgenomic	706025
Amaxa Human Stem Cell Nucleofector Kit 2	Lonza	VPH-5022
DNeasy Blood and Tissue Kit	QIAGEN	69504
PCRx enhancer system	Invitrogen, Life Technologies	11495017
TOPO-TA cloning kit	ThermoFIsher	451641
QIAprep Spin Miniprep Kit	QIAGEN	27106
Seahorse XF Cell Mito Stress Test Kit	Agilent	103015-100
Experimental Models: Cell Lines		
HeLa cells	N/A	N/A
Experimental Models: Organisms/Strains		
SCA7 266Q mice	H. Zoghbi	Yoo et al., 2003
Oligonucleotides		
NMNAT1 Taqman probe	Life Technologies	Hs00978912_m1
ATXN7 gRNA (CGGGCCGCGGATGACGTCAGG)	Life Technologies	Customized GeneArt DNA string
SCA73.1F 5′-GAGCGGAAAGAATGTCGGAGCG-3′	IDT	N/A
SCA73.327R 5′-CAGGAACTTTGGAAGCCTCAACCC-3′	IDT	N/A
Recombinant DNA		
Oct4, Sox2, Klf4, c-Myc plasmids (Yamanaka factors)	A. Muotri	Chailangkarn et al., 2016
pUC57 N/A	A. Muotri	Thomas et al., 2017
CMV::Cas9-2A-eGFP	Addgene	RRID:Addgene_44719
CMV::Cas9D10A-2A-EGFP		RRID:Addgene_44720
EGFP-2A-puroR-2A	This paper	N/A
EGFP-2A-puroR-2A-Atxn7cDNA (10 CAG)	This paper	N/A
EGFP-2A-puroR-2A-Atxn7cDNA (113 CAG)	This paper	N/A
Cytoplasmic NAD sensor	L. Cambronne	Cambronne et al., 2016
Nuclear NAD sensor	L. Cambronne	Cambronne et al., 2016
Mitochondrial NAD sensor	L. Cambronne	Cambronne et al., 2016
Cytoplasmic cpVenus control	L. Cambronne	Cambronne et al., 2016
Nuclear cpVenus control	L. Cambronne	Cambronne et al., 2016
Mitochondrial cpVenus control	L. Cambronne	Cambronne et al., 2016
Software and Algorithms		

REAGENT or RESOURCE	SOURCE	IDENTIFIER
MitoDB database	Scheibye-Knudsen et al., 2013	www.mitodb.com
GraphPad Prism	GraphPad Software	N/A
ImageJ	N/A	https://imagej.nij.com/ij/
ImageJ mitochondrial morphometry plugin	Dickey and Strack, 2011	From author
cnvPartition progra	Illumina	N/A
gada R package		http://www.creal.cat/jrgonzalez/software.htm#ancla-MAD
E-CRISP design site	Heigwer et al., 2014	http://www.e-crisp.org/E-CRISP/
SigmaPlot	Systat Software	https://systatsoftware.com/
Origin	Origin Labs	https://www.originlab.com/
galaxy workflow4metabolomics	Giacomoni et al., 2015	https://galaxy.workflow4metabolomics.org/